Appl. Phys. A (2014) 117:1727–1747
DOI 10.1007/s00339-014-8763-y

Applied Physics A
Materials Science & Processing

INVITED PAPER

Focused helium-ion-beam-induced deposition

P. F. A. Alkemade · H. Miro

Received: 22 May 2014 / Accepted: 29 August 2014 / Published online: 24 September 2014
© Springer-Verlag Berlin Heidelberg 2014

Abstract The recent introduction of the helium ion microscope (HIM) offers new possibilities for materials modification and fabrication with spatial resolution below 10 nm. In particular, the specific interaction of He^+ ions in the tens of keV energy range with materials—i.e., minimal deflection and mainly energy loss via electronic excitations—renders the HIM a special tool for ion-beam-induced deposition. In this work, an overview is given of all studies of helium-ion-beam-induced deposition (He-IBID) that appeared in the literature before summer 2014. Continuum models that describe the deposition processes are presented in detail, with emphasis on precursor depletion and replenishment. In addition, a Monte Carlo model is discussed. Basic experimental He-IBID studies are critically examined. They show deposition rates of up to 0.1 nm^3/ion. Analysis by means of a continuum model yields the precursor diffusion constant and the cross sections for beam-induced precursor decomposition and beam-induced desorption. Moreover, it is shown that deposition takes place only in a small zone around the beam impact point. Furthermore, the characterization of deposited materials is discussed in terms of microstructure and resistivity. It is shown that He-IBID material resembles more electron-beam-induced-deposition (EBID) material than Ga-ion-beam-induced-deposition (Ga-IBID) material. Nevertheless, the spatial resolution for He-IBID is in general better than for EBID and Ga-IBID; in particular, proximity effects are minimal.

P. F. A. Alkemade (✉) · H. Miro
Kavli Institute of Nanoscience, Delft University of Technology, Lorentzweg 1, 2628 CJ Delft, The Netherlands
e-mail: p.f.a.alkemade@tudelft.nl

1 Introduction

1.1 Focused electron and ion beams for imaging and nanofabrication

Many medium or large laboratories in the natural sciences possess one or several scanning electron microscopes (SEMs). The main use is of course imaging, and the most advanced SEMs offer nowadays an imaging resolution of about 1 nm. An essential factor that limits resolution is diffraction, which is rooted in the fundaments of nature and, therefore, cannot easily be mitigated, unless one shifts to higher electron energies. Ions have higher momentum and thus shorter wavelength than electrons of the same energy. Therefore, a focused ion beam (FIB) can in principle provide higher imaging resolution than a focused electron beam (FEB). However, two important factors obstructed widespread use of FIBs for imaging. First, the brightness (i.e., the number of particles emitted per unit of source area and per unit of steradian) of the available sources was limited. Until recently, almost all commercial FIB instruments have a liquid metal ion source (LMIS) of Ga^+. The limited brightness implied a practical probe size of at best 5 nm [1]. The second obstruction is the inherent damage by the heavy Ga^+ ions. Often, the surface is destroyed by ion sputtering before a useful image could be taken. In fact, Ga-FIBs became popular precisely because of the possibility of local sputtering, or nanomachining [2]. Since the late 1980s, the main use of FIBs is ion beam materials processing; initially for electronic circuit edit and repair of lithographic masks, later for fabrication of lamellae for transmission electron microscopy (TEM), cross sectioning for subsurface materials analysis, and prototyping nanoscale devices.

The presence of a gas during a FEB or FIB bombardment can lead to beam-induced decomposition of adsorbed gas molecules. The molecules decompose when excited by an incident primary beam particle or by one of the secondary particles. Some molecular fragments are volatile and disappear in the environment of the instrument, whereas others form bonds with the atoms in the substrate. As a consequence of the latter process, a deposit grows at and near the spot where the focused beam hits the surface. This process can be used to grow nanoscale objects, and numerous examples are discussed in the present volume, e.g. in the review by van Dorp [4]. Figure 1 is an example of parallel platinum lines grown by He^+-ion-beam-induced deposition (IBID).

Although the gallium LMIS is widespread for nanomachining, the need for FIBs for imaging remained. A concept explored over several decades by various groups was the gas-field ion source (GFIS), using noble gas atoms, thus avoiding detrimental Ga-contamination and excessive damage [5–7]. After many years of research and development, the US-based company ALIS manufactured in 2006 a commercial scanning ion microscope with a focused He^+ ion beam from a GFIS [8, 9]. Most important characteristics of the He^+ GFIS are a very high brightness and reasonable source stability and lifetime. This instrument, named Orion and now available from Carl Zeiss, can produce a 30-keV He^+ beam of several picoamperes and a probe size of <1 nm [7]. Although the company's objective was ion microscopy, various groups explored the instrument's potential for nanofabrication, either via ion beam lithography [10–13], ion milling [14–20], IBID [7, 16, 21], or ion-beam-induced etching [22].

Various overview articles on helium-ion-beam nanofabrication have appeared in recent years [3, 7, 22–27]. The present chapter is a review of the published studies on nanofabrication via helium-ion-beam-induced deposition (He-IBID). All studies have been executed on Orion Plus helium ion microscopes (HIMs). The field is still mainly in an explorative phase, and so far only a handful of chemistries has been investigated. Nevertheless, it has become clear that between the established techniques of electron-beam-induced deposition (EBID) and Ga-ion-beam-induced deposition (Ga-IBID), He-IBID has unique characteristics, combining advantages of both. But the most striking unique characteristic is the high spatial precision at which materials can be grown, without any noticeable overspray or proximity effects. The example of Fig. 1 demonstrates a precision in the ten-nanometer range, but better results have been achieved in thinner deposits [22].

Because of the newness of this field, this review offers in principle the possibility to be 'complete.' Hence, besides listing hopefully all publications to date, we aim to discuss these publications' main results as well. Specifically, we will focus on modeling, since that subject has received little attention so far, apart from extensive Monte Carlo modeling [28].

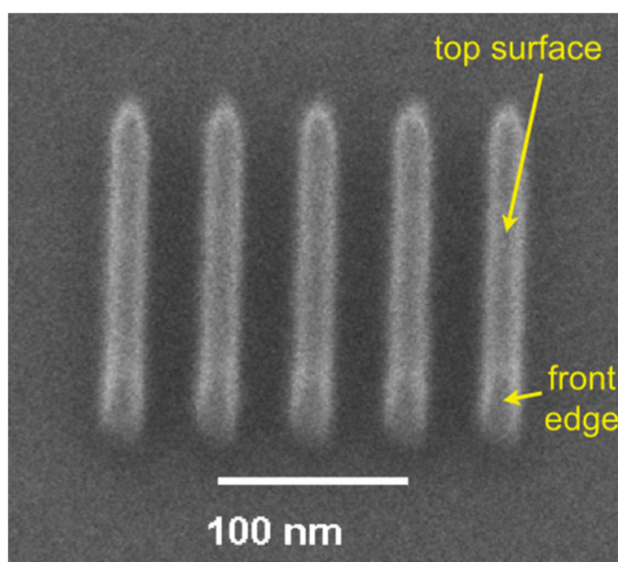

Fig. 1 Bird's-eye helium ion microscopy (HIM) image of platinum lines, deposited with He-ion-beam-induced deposition (He-IBID); sample tilt is 30°. During the deposition, the 25-keV and 2-pA He^+ beams was moved repeatedly along five parallel single-pixel lines. The grown PtC_x lines are 15 nm wide and 50 nm high. Reprinted with permission from [3]. Copyright 2010 Society of Photo Optical Instrumentation Engineers

A multitude of processes is involved in beam-induced deposition. Since acquaintance with these processes is indispensable for understanding experimental studies and applications, we give first an overview of the current knowledge of these fundamental processes. Fortunately, it turns out that He-IBID is simpler than its counterparts EBID and Ga-IBID. Then, we will describe two analytical models of He-IBID and subsequently describe a few fundamental He-EBID studies. We will use the analytical models to analyze measured deposition rates. Next, we will summarize characterization of He-IBID materials and then compare He-IBID with EBID, Ga-IBID, and Ne-IBID. We will end this chapter by summarizing the main characteristics of He-IBID.

2 Fundamentals

2.1 Ion–matter interactions

When energetic ions travel trough a solid, they transfer their kinetic energy to the atoms in the solid. In general, two different processes determine the ion's energy loss: (1) energy loss by interaction with the nuclei of the atoms and (2) energy loss by atomic excitations. At energies above

1 keV, the energy transfer can be regarded as a series of successive two-body collisions. The process of energy transfer from ions to solids is described in numerous overview articles and books and in various handbooks. A good example of the latter is the series by Ziegler et al. [29]. The review by Volkert and Minor [2] describes the processes during (Ga^+) FIB bombardment. Here, we will summarize only the aspects relevant for this review.

The interaction during the collision is governed by the screened Coulomb force between the nuclei of the two particles. After the collision, the ion and the recoiled atom are in motion, and both will collide with other atoms, resulting in a cascade of atomic collisions. In the cascade, the original kinetic energy of the ion is distributed over typically 10^5–10^6 atoms. As a consequence, many bonds in the material near the ion's trajectory are broken, the material is being mixed and, sometimes, amorphized. Finally, the ion comes to rest, and most of the deposited energy is dissipated as heat to the material or its surroundings. Because the Coulomb force depends on the nuclear charge, the energy loss of heavy ions in matter is larger than for light ions of the same velocity.

The moving ion also excites and ionizes atoms and, hence, loses extra energy. Whereas nuclear collisions result in the direct physical breakup of atomic bonds, atomic excitations can lead to unstable and subsequently broken bonds, i.e., molecular dissociation. Moreover, the ion can capture and lose electrons or produce a collective excitation of the electron plasma of the solid. The maximum energy transfer of an ion of mass M and kinetic energy E_0 to a free electron at rest is $4E_0m_e/M$, where m_e is the electron mass. For 30 keV He^+, it is 16 eV.

Energetic particles that reach the surface can escape from the solid. One calls the escape of recoiled atoms during ion-beam bombardment 'ion milling' or 'sputtering' and the escape of electrons 'secondary electron (SE) emission.' Figure 2a shows these secondary particle emission processes. Sputtering yields for a 30-keV Ga^+ beam—the most common FIB—are usually between 1 and 5 removed atoms per incident ion for perpendicular incidence, but at oblique incidence, the yields can be several times higher. In He^+-beam bombardment, sputtering yields are about 10–50 times lower than for Ga^+ bombardment [30]. SE yields for both ions are similar, typically several electrons per ion, and, indeed, the measured SE energy for 30-keV He^+-beam bombardment is less than the free-electron limit of 16 eV [31]. A distinction is often made between two types of SEs: SE1's are the SEs generated by incident primary ions and SE2's are those generated by backscattered ions or recoiled atoms.

For 30-keV Ga^+, the average energy loss per distance travelled in, e.g., silicon, is 1,100 eV/nm by nuclear collisions and 120 eV/nm by electronic excitations [29]. The much lighter He^+ loses little energy by nuclear collisions, only 8 eV/nm in silicon, whereas the loss by electronic excitations is 100 eV/nm. The total energy loss of He^+ is thus about an order of magnitude lower than of Ga^+, and hence, He^+ penetrates materials typically ten times as deep, e.g., 300 nm in silicon. Moreover, because nuclear interactions of He^+ ions are relatively weak and because interactions with individual electrons do not transfer much

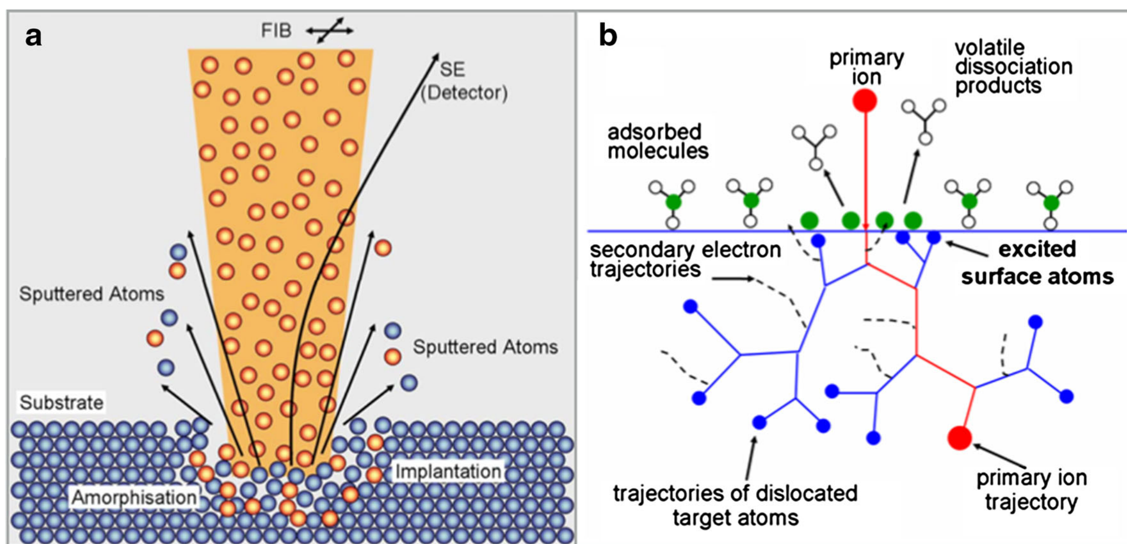

Fig. 2 **a** Principle of FIB milling or sputtering and secondary electron (SE) emission. Note that the amorphized surface region contains implanted primary ions. **b** Interactions of a primary heavy ion in a solid, producing SE's and dislocated target atoms in a collision cascade. It is assumed that the excited surface atoms cause adsorbed molecule dissociation. Reprinted with permission from [32, 33]. Copyright 1994 and 2008 American Vacuum Society

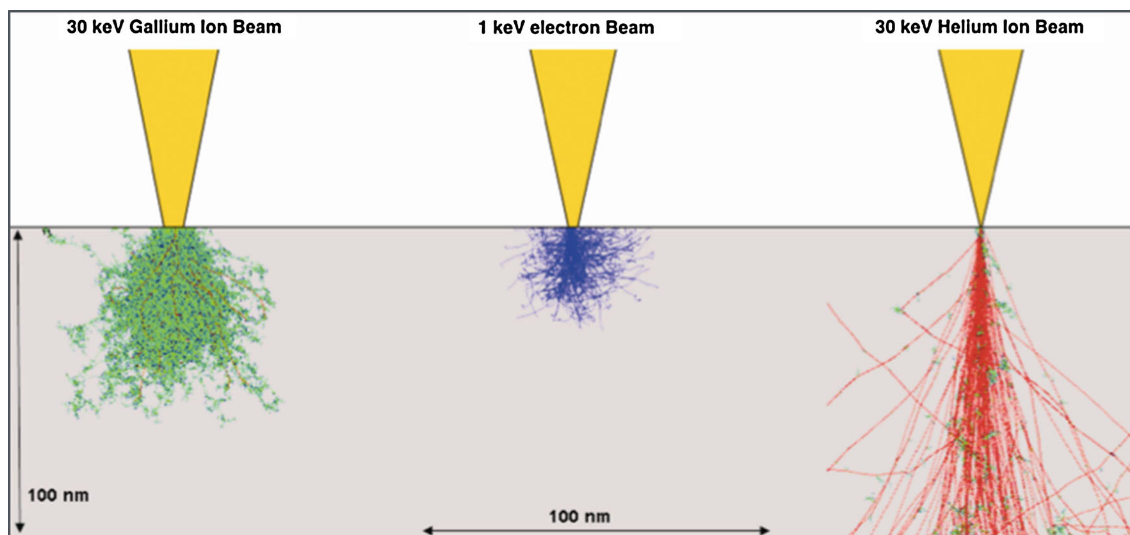

Fig. 3 Simulated trajectories of 30 keV Ga^+, 1 keV electrons, and 30 keV He^+ in Si. Note the deep penetration, the weak deflections, and the absence of backscattering of the He^+ ions. Reprinted with permission from [34]. Copyright 2007 American Institute of Physics

momentum, deflections of He^+ ions are small and the ions travel mainly along straight trajectories. The simulated trajectories of Ga^+ ions, electrons, and He^+ ions in Fig. 3 show an essential and favorable aspect of He^+-ion microscopy and nanofabrication: Perpendicularly incident He^+ ions rarely return to the surface of a flat specimen and therefore almost all beam-induced surface processes, in particular SE emission, occur at or near the beam entrance point. In contrast, the numerous backscattered Ga^+ ions and electrons induce surface processes also at large distances from the beam entrance point.

2.2 Processes at a dynamic surface

Bond breaking, mixing, and sometimes new compound formation occur also at the surface of the bombarded material. However, the surface has a different composition and history than the bulk, because its physical and chemical states are also dictated by the gaseous, liquid, or vacuum environment of the material. Moreover, these states are dynamic. For instance, continuous adsorption of water or hydrocarbon molecules during bombardment can change the surface condition, even if the ion beam is constantly removing atoms from the surface. Moreover, if the supply of atoms from the gas phase exceeds their sputter removal, net growth of material takes places. The process of beam-induced growth or deposition has been known from the early days of electron microscopy and ion beam analysis. Often unwanted carbonaceous layers were formed by decomposition of adsorbed hydrocarbon molecules from pump-oil vapors or contaminated surfaces in the vacuum system.

The continuous supply and removal of molecules from the gas phase, of particles from the ion beam, and of atoms from the bulk make the processes at an ion-beam-bombarded surface very dynamic and complex. A small change in a few of the conditions—e.g., in the amount of supply, transport, or removal—can cause a major change in the composition or shape of the evolving surface. In its turn, changes in surface composition and shape can affect the supply, transport, and removal rates. It is evident that one can use ion beam bombardment to induce useful surface reactions of selected precursor molecules. However, the dynamic and complex nature of these surface processes makes systematic optimization cumbersome or worse. Nevertheless, one has studied ion-beam-induced surface reactions for this purpose since the early days of FIB materials modification, see, e.g., the review on gas-assisted focused beam processing and fabrication by Utke et al. [33].

2.3 Simple structures made by He-ion-beam-induced deposition

Movements of the ion beam during the decomposition of continuously adsorbing precursor gas molecules result in a complex, three-dimensional deposit. Its shape resembles the beam movement, but they are not identical.

The five lines of Fig. 1 are grown via decomposition of trimethyl (methylcyclopentadienyl)-platinum [or MeCpPtMe$_3$ or $(CH_3)_3Pt(C_PCH_3)$] [3]. MeCpPtMe$_3$ is a common metalorganic precursor gas used in EBID, IBID, chemical vapor deposition (CVD), and atomic layer deposition (ALD). Its chemical composition is PtC_9H_{16}. The specimen of Fig. 1 was tilted 30° during imaging in order to show the

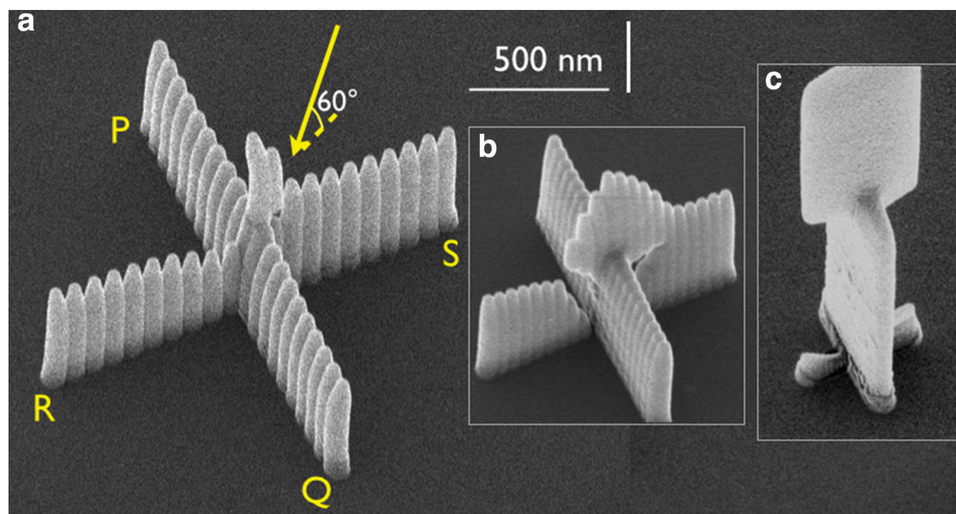

Fig. 4 Crosses formed by two He-IBID walls of 21 pillars at **a** 75-, **b** 50-, and **c** 20-nm separation. The *PQ* wall was grown first. The *arrow* indicates the direction of the flux of $MeCpPtMe_3$ precursor molecules from the gas injection needle. Blocking of arriving precursors and deposition outside the beam impact point determine to a large extent the shape. Reprinted with permission from [24]. Copyright 2012, John Wiley and Sons

front edge—and, thus, the height—of the lines. During deposition, the substrate surface was oriented perpendicular to the ion beam. Note that the two outer lines have the same dimensions as the inner lines and that all sidewalls are almost vertical. There is, thus, a good one-to-one relationship between the pattern of the beam movements and the shape of the deposit, although the actual lines are wider than the lines of the pattern. In other words, proximity effects are present, but they are minor.

To make the structures of Fig. 4, a 25-keV and 0.2-pA He^+ ion beam was moved repeatedly in 21 steps from *P* to *Q* and then repeatedly in the perpendicular direction from *R* to *S* [24]. The beam step size was 20, 50, or 75 nm, and the dwell time was always 50 µs. The precursor gas was $MeCpPtMe_3$. The ion beam with a diameter of about 1 nm was incident parallel to the surface normal, and the flow of the precursor molecules was at an angle of 60° to the surface, see the arrow in Fig. 4a. Despite the small beam diameter and the large step size, the structures are two intersecting continuous walls: growth did not happen only at the 41 beam impact points. Moreover, the shape is not a simple cross. Apparently, blocking of the supply of precursors by the first wall between *P* and *Q* caused a depression in the segment of the second wall between the center and *R*. Obviously, the peak in the center is caused by the growth of part of the second wall on top of the first one. The growth of nearly the entire second wall on top of the first in Fig. 4c can be understood as lateral outgrowth of the central peak. Note the small 'feet' in the *R*–*S* direction, likely grown before the second wall reached its full breadth.

Structures grown by EBID, He-IBID, and Ga-IBID do not differ much. The physical mechanism that induces the decomposition of the precursor molecules is transfer of kinetic energy of the incident ions or electrons to the adsorbed molecules. Because the nature of the energy transfer can be different for electrons, light ions, and heavy ions, one can expect differences in the deposits. For example, there might be differences in composition, deposition efficiencies (deposited volume per unit of charge), minimal feature sizes, stray deposition, or halos. We will describe possible and observed differences later in this review.

3 Models of He-IBID

3.1 A sketch

The physical and chemical processes during IBID are not exclusive for EBID or IBID, nor rarely studied. Nevertheless, their complex interplay hampers quantitative and predictive modeling of IBID as a growth technique. Process optimization is still mainly based on trial-and-error, guided by guesses, qualitative understanding, and approximated modeling and computer simulations.

Although the set of parallel lines of Fig. 1 is a very simple structure, understanding all growth processes during IBID is, thus, not trivial at all. In order to give the reader an idea of the complex interplay, we sketch in this section a relatively simple example: the growth of a line as thin as possible and of limited height. The focused helium ion beam is moved along a linear set of spots on a flat substrate surface. The beam has a Gaussian shape with a full width at half maximum of d_b. After a dwell time τ_d in one spot, the beam moves to the neighboring spot. The time to make this step is much shorter than τ_d, and the size of the step is considerably less than d_b. We assume that precursor molecules stream out from the orifice of a gas injection needle and hit the surface in a wide zone around the beam impact area. Furthermore, if a molecule hits an empty surface site, it might stick; otherwise, it is reflected back into the gaseous environment.

The cross-sectional and top-view sketches in Fig. 5 depict the important processes. The incident beam is highly focused with a decreasing intensity at its flanges. The width of the growing line is much larger than the width d_b of the beam. The gas injection needle is to the left, outside the sketched region. The inhomogeneous density of the adsorbed precursors is shown as a blue layer of variable thickness in Fig. 5a and of variable 'blueness' in Fig. 5b. This inhomogeneity is caused by precursor depletion by beam-induced reactions and by blocking of incoming precursor molecules by the deposit itself: The deposit's right slope and the adjacent substrate surface are located in the 'shadow' of the deposit. In this depletion zone, IBID is rare, and hence, most growth takes place off-center of the beam.

Some impinging molecules are reflected (Refl) when they hit the surface, whereas other adsorb (Ads). Surface diffusion (Dif) of adsorbed molecules takes place as well, thus reducing differences in their densities, and some adsorbed molecules desorb via thermal activation (TDes). Excitation by the penetrating ions can cause precursor decomposition in the beam spot. Decomposition is sketched as black-purple stars in Fig. 5. The excitation might, however, also cause precursor desorption (BIDes). During passage of the surface, some SEs cause decomposition, often outside the beam spot. Also other energetic atoms and escaping deflected He^+ ions can cause precursor decomposition outside the actual beam spot. A few reentering SEs cause decomposition at a distance from the deposit, and one reaction in the gas phase (GPR) is shown; its product might land anywhere on the substrate or the deposit.

Fragments of decomposed precursor molecules might either desorb or bind chemically to the surface and become incorporated in the deposit. The width of the thus growing deposit is determined by the width of the ion beam, the scattering of the ions in the deposit, and the distance the SEs and recoiled atoms can travel before they reach the adsorbed precursor layer. Although backscattering is rare, deflected He^+ ions can easily reach the edge of a narrow and high structure.

The transfer of the energy from the beam to secondary particles, the spread of the primary and secondary particles, and the transport of precursor molecules all determine the growth of the deposit. Since the geometry evolves, not all these processes are constant. In-depth understanding of the influence of these processes can be obtained by mathematical analysis.

3.2 Mathematical description of He-IBID

To give the reader a sense of the interdependencies of the involved processes, we present below a mathematical model of He-IBID. The approach follows Ref. [33].

We describe the fluxes of primary and secondary particles, labeled i, with the energy, position, and time-dependent functions $f_i^*(E, \vec{r}, t)$ and $f_i(\vec{r}, t)$. We assume that all fluxes f_i are proportional to the primary beam current i_{PI} ($= e \times F_{PI}$, where F_{PI} is the integrated flux of the primary beam). Then, the probability P per unit of time for decomposition reaction of a given precursor molecule at surface position $\vec{r}$ via excitation by any energetic particle is:

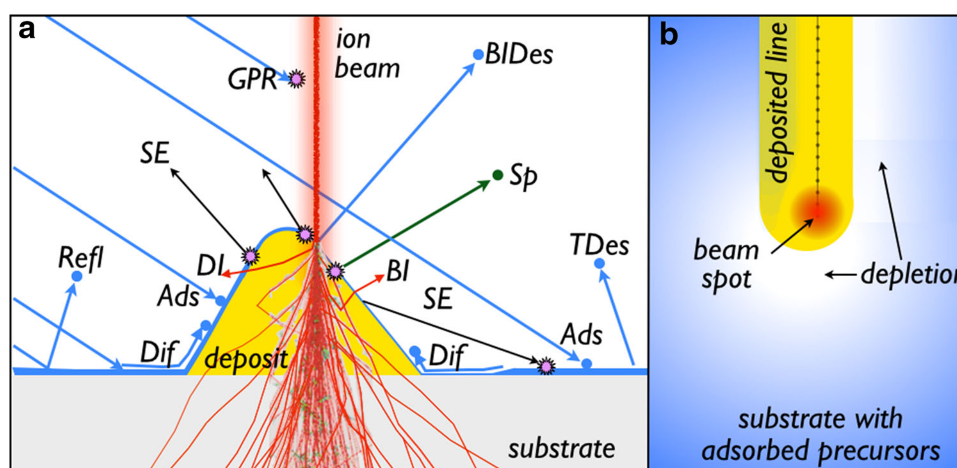

Fig. 5 **a** *Cross-sectional* view and **b** *top* view of He-IBID of a line. The precursor molecules (*blue*) enter from the *left*. The beam (*red*) is in the last point at the end of a series (*black dots* on the *vertical line* in **b**). *BI* backscattered ion, *DI* deflected ion, *Dif* diffusing precursor, *Ads* adsorption, *Refl* reflection, *TDes* thermal desorption, *BIDes* beam-induced desorption, *Sp* sputtering, *GPR* gas-phase reaction. *Black-purple stars* are particle-induced precursor decomposition events, occurring at various places and induced by various (primary and secondary) particles. The *blue* layer is the adsorbed precursor layer; its thickness is inhomogeneous

$$P(\vec{r},t) = \sum_i \int \sigma_i(E) f_i^*(E,\vec{r},t)\mathrm{d}E = \sum_i \sigma_i^{\mathrm{eff}} f_i(\vec{r},t) \quad (1)$$

where $\sigma_i(E)$ is the cross section for the decomposition by particles of type i and energy E. The type can refer to primary He^+ ions (PI), re-emitted backscattered (BI) or deflected (DI) He^+ ions, energetic (EA) or sputtered (SP) atoms, and SEs.

The decomposition rate q_{dep} at $\vec{r}$ is:

$$q_{\mathrm{dep}}(\vec{r},t) = \sum_i n(\vec{r},t)\sigma_i^{\mathrm{eff}} f_i(\vec{r},t) = n(\vec{r},t)P(\vec{r},t), \quad (2)$$

where n is the surface density of the adsorbed precursors. The deposition rate g_{dep}—expressed in volume per unit of time—is $g_{\mathrm{dep}} = V_{\mathrm{p}}\, q_{\mathrm{dep}}$, with V_{p} the deposited volume per decomposed precursor.

The change $\partial n/\partial t$ of the surface density depends on the local flux j_{tot} of impinging precursor molecules, the maximal possible density n_0 of adsorbed precursors, the actual density n, the probability s of sticking of a precursor impinging onto an empty site, the thermal desorption rate τ_{des}, effective reaction cross sections σ_i^{eff}, the cross sections for beam-induced desorption σ_i^{des}, the fluxes f_i of energetic primary and secondary particles, and the precursor diffusion constant D:

$$\frac{\partial n}{\partial t} = s j_{\mathrm{tot}}\left(1 - \frac{n}{n_0}\right) + D\nabla^2 n - \frac{n}{\tau_{\mathrm{des}}} - n\sum \sigma_i^{\mathrm{eff}} f_i - n\sum \sigma_i^{\mathrm{des}} f_i. \quad (3)$$

Note that quantities depend on the surface composition at $\vec{r}$. In practice, there are only two extreme compositions present: that of the substrate and of the deposit. However, local mixtures can exist as well, albeit temporary. Two important steady-state growth regimes can be derived from Eq. (3). For simplicity, we assume here that diffusion and desorption are negligible (D, σ_i^{des} and $1/\tau_{\mathrm{des}} \to 0$). Then, in steady state ($\partial n/\partial t = 0$):

$$n\sum_i \sigma_i^{\mathrm{eff}} f_i = s j_{\mathrm{tot}}\left(1 - \frac{n}{n_0}\right) \quad (4)$$

If the fluxes f_i of energetic particles are large, n must be small. If $n \ll n_0$,, we have $n\sum \sigma_i^{\mathrm{eff}} f_i \approx s j_{\mathrm{tot}}$. Then, the deposition rate g_{dep} depends via n only on the precursor flux j_{tot}. This growth regime is called the precursor-limited regime [33]. If on the other hand the energetic particle fluxes f_i are low, n approaches n_0 and the deposition rate g_{dep} is proportional to $n_0 \sum \sigma_i^{\mathrm{eff}} f_i$. The only practical method to increase g_{dep} is then to increase all fluxes f_i, i.e., to increase the primary ion current i_{PI}. This growth regime is called the ion-limited regime.

The inclusion of diffusion and desorption affects the regimes, but not in essence. If the main supply of precursors to the reaction zone is not by direct adsorption but by diffusion from the surrounding areas, one calls this regime the diffusion-enhanced precursor-limited regime. Note that in and close to the beam impact zone, deposition rates are high and consequently the precursor density n low. Here, often the precursor-limited regime holds, while the ion-limited regime holds at larger distances to the beam impact zone.

The impinging precursor flux j_{tot} depends on the surface orientation at $\vec{r}$. We define $\hat{p}(\vec{r},t)$ as the local surface normal and $\vec{j}_0$ as the vector representing the magnitude and direction of the flux from the gas injection needle. If there is unhindered flow, the impinging flux j is:

$$j(\vec{r},t) = -\vec{j}_0 \cdot \hat{p}(\vec{r},t) = |j_0 \cos\theta(\vec{r},t)| \quad (5)$$

where $\theta(\vec{r},t)$ is the angle between the local surface normal and the gas injection needle. The molecular flow expands in the open region between the needle and the substrate [33], and therefore, one must add a spreading function, $\mu_n(\vec{r})$, to Eq. (5).

Objects located between the needle and the beam impact region might block the impinging molecules. The amount of blocking can be represented by a function $b_n(\vec{r},t)$, which is 0 for no blocking and 1 for complete blocking. For instance, the right slope of the deposit in Fig. 5 and the adjacent substrate region cannot be reached directly by molecules from the needle; that part is in the shadow. On the other hand, scattering of molecules in the gas phase or reflection from other surfaces can contribute as a background precursor flux j_{bgr}.

Hence, the total impingement rate of precursors is:

$$j_{\mathrm{tot}}(\vec{r},t) = j_0\mu_n(\vec{r})(1 - b_n(\vec{r},t))\cos\theta(\vec{r},t) + j_{\mathrm{bgr}}(\hat{p}(\vec{r},t)). \quad (6)$$

Even for constant flow j_0, the impinging precursor flux $j_{\mathrm{tot}}(\vec{r},t)$ is time dependent via the developing local surface normal $\hat{p}(\vec{r},t)$, the blocking function $b_n(\vec{r},t)$, and the background gas flux j_{bgr}. Furthermore, the sticking s in Eq. (4) might depend on the changing local composition.

The amount of ion beam sputtering g_{sp} (in nm^3/s) depends on the local composition, the flux of primary ions, and the local orientation of the surface:

$$g_{\mathrm{sp}}(\vec{r},t) = -Y_{\mathrm{A}}(\hat{p}(\vec{r},t))V_{\mathrm{A}} f_{\mathrm{PI}}(\vec{r},t), \quad (7)$$

where Y_{A} is the sputtering yield (number of sputtered atoms per incident ion) for material A and V_{A} the volume per atom. The sputtering yield depends on the angle θ between the incident beam and the local surface normal. For 25-keV He^+ on most materials, the sputtering yield increases from typically 0.05 at 0° to ~0.5 near 80° and then drops quickly to zero at 90° [30].

Hence, the local change in volume per unit of time is:

$$g_{\mathrm{tot}}(\vec{r},t) = \sum_i \left(n(\vec{r},t)V_{\mathrm{p}}\sigma_i^{\mathrm{eff}}f_i(\vec{r},t)\right) - Y_{\mathrm{A}}(\hat{p}(\vec{r},t))V_{\mathrm{A}}f_{\mathrm{PI}}(\vec{r},t). \quad (8)$$

Deposition and sputtering are, however, not the only processes that change the shape and volume of the deposit and the substrate. Thermal and beam-enhanced diffusion can change the shape. And implantation of primary ions increases the volume, unless the implanted ions are able to diffuse out. However, the range of implanted He^+ ions is often hundreds of nanometers, and implantation affects mainly the volume over large distances in the substrate [35].

Although one can write differential equations for the relevant processes, in all but the most trivial cases a straightforward analytical solution for Eqs. (2) or (8) cannot be found. Moreover, minor changes in conditions can change the outcome of a deposition job drastically. If, for instance, the supply of precursors is locally reduced by shadowing, material removal by sputtering can exceed deposition. Then, the area sinks with respect to the surrounding material and becomes even less accessible to precursors, amplifying the deviation from a flat surface. The dip in the left section of the cross in Fig. 5a, b is an example of a shape that is strongly affected by shadowing.

The interdependent functions of Eqs. (2), (3), (6), and (7) and their strong temporal and spatial dependencies make solving Eqs. (2) and (8) for many practical deposition jobs enormously complex. Nevertheless, a continuum solution for simple systems is very instructive.

3.3 Continuum models for simple cases

In Ref. [36], a simple analytical model for the growth of pillars in He-IBID with a stationary beam was presented. Figure 6 shows pillars grown with (a) a Ga^+ beam and (b + c) He^+ beams of various currents. The Ga-grown pillar is broad—160 nm—and has many side lobes. In contrast, the He pillars are much narrower and smoother.

The highest and narrowest ones are obtained at the lowest currents; the narrowest is 35 nm in diameter. Despite the large difference in ion mass, the volumetric growth rates are comparable: 0.05 nm^3 per Ga^+ ion and 0.03–0.05 nm^3 per He^+ ion. After the initial phase, the growth rates of all pillars did not change [36, 37]. Apparently, precursor diffusion from the substrate along the pillar shaft to the reaction zone is not the rate-limiting step.

Figure 7a shows a TEM image of the top of one pillar. The radius of curvature, r_c, is 9 nm. The primary and secondary reaction zones (RZ1 and RZ2) are indicated. In Fig. 7b, we sketch a growing pillar, partly covered by precursor molecules (green spheres surrounded by four small black spheres). Note the large precursor depletion in RZ1. Two He^+ trajectories are depicted (dark yellow in vacuum and gray in the pillar). Both ions are deflected and escape from the pillar. SE (SE1) emission at the ion's entrance causes precursor decomposition (purple star) in the primary reaction zone RZ1; the corresponding vertical growth speed is v_V. SE (SE2) emission causes decomposition at the flanges, thus in the secondary reaction zone RZ2; the lateral growth speed is v_L. The total range of (undeflected) He^+ ions in the pillar is R. In this phase of growth, the only development is a constant rise of the top part of the pillar. Beyond R, the pillar width w remains constant during the remainder of the deposition job.

The pillars of Fig. 6b, c grown at the high currents are relatively short. Apparently, depletion at the apex reduced the vertical growth speed v_V. The growth was analyzed assuming only decomposition by SE1 (leading to vertical

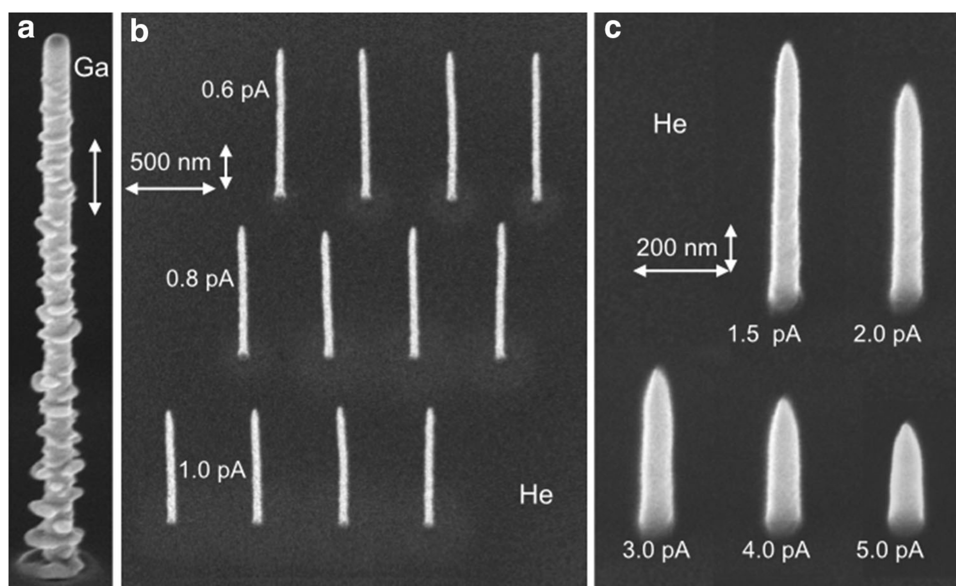

Fig. 6 **a** Pt pillar grown with a stationary 1-pA and 30-keV Ga^+ beam; ion dose is 180 pC [37]. **b**, **c** Pt pillars grown with a stationary 25-keV He^+ beam at various currents; ion dose is 6 pC. The viewing direction is **a** 60° and **b**, **c** 30° to the pillar axis. **a**, **b** Have the same *horizontal scale*. Modified by permission from [38]. Copyright 2010 IOP Publishing

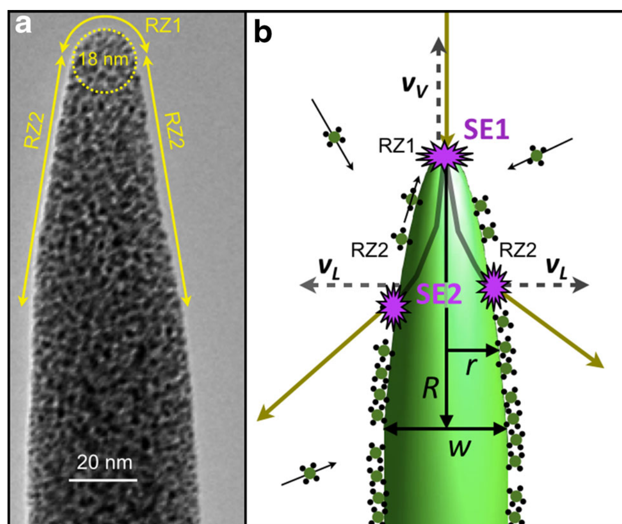

Fig. 7 **a** Bright-field TEM image of a Pt pillar grown by He-IBID. The apex has a radius of curvature, r_c, of 9 nm. Two distinctive reaction zones are depicted: RZ1 and RZ2. **b** Sketch of a pillar growing by beam-induced decomposition of adsorbing and diffusing precursor molecules; the vertically incident ion beam is stationary. Courtesy (**a**) Frans Tichelaar, TU Delft. **b** Modified with permission from [39]. Copyright 2011 American Vacuum Society

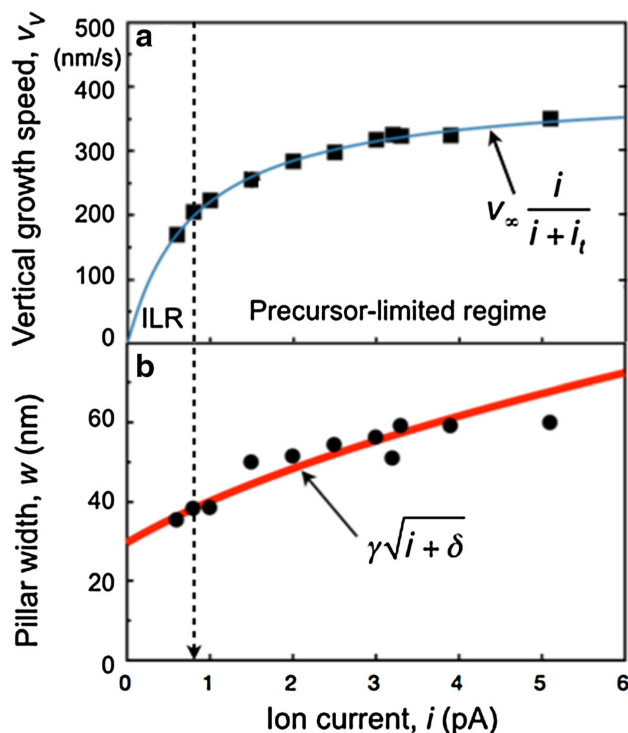

Fig. 8 Relation between **a** vertical growth speed and **b** pillar width and He^{+} current for the pillars of Fig. 6b, c. Full *curves* are analytical fits discussed in the text. *Dashed line* indicates i_t. Modified with permission from [36]. Copyright 2010 American Vacuum Society

growth) and SE2 (leading to lateral growth) [36]. A steady-state continuum model for the transition of the ion-limited regime to the precursor-limited regime [33, 40] can describe the measured saturation of the vertical growth speed, see the fit curve in Fig. 8a. Fit parameters were v_∞ and i_t. Figure 8b shows how the pillar broadens with increasing ion current i. Alkemade et al. [36] used the continuum model plus the assumption that at currents below 6 pA ($\sim 7i_t$) depletion at the flanges is still negligible. They showed that the pillar radius r within the ion range R (see Fig. 7b) grows as:

$$\frac{\mathrm{d}r}{\mathrm{d}t} = \frac{k_s i}{2r}, \tag{9}$$

where the constant k_s includes the precursor surface density n, the SE2 generation rate, and the cross section σ_{SE} of decomposition by low-energy electrons. Note that the rate decreases as r^{-1} because the pillar's circumference is increasing, and therefore, the same number of energetic particles is spread out over a larger region. Integration over the time available for pillar broadening ($=R/v_v$) yields a relation between the final pillar width w and the ion current i:

$$w(i) = 2\sqrt{\frac{k_s(i+i_0)R}{v_\infty} + r_0^2} = \gamma\sqrt{i+\delta} \tag{10}$$

The constants γ and δ have been fitted to the experimental data; the result is the red curve in Fig. 8b. At higher currents (>3 pA), the experimental width seems to saturate faster than calculated. Probably, the precursor-limited regime proliferates from the apex down to the flanges, slowing down the lateral growth as well. It was concluded in Ref. [36] that both the ratio between SE1 and SE2 emission and the ratio between the precursor coverage at the apex and at the flanges determine the ratio of vertical and lateral growth speeds. The latter ratio determines the final width of the pillar.

Utke et al. [41] developed an analytical continuum EBID/IBID model for a stationary beam and a flat deposit, i.e., a deposit much lower than wide. In that case, the mathematics is 2-D or, because there is rotational symmetry, 1-D. The authors show that the ratio between the diameters of the deposit and the beam is a function of the ratio between the maximal ion or electron flux and the precursor flux, the ratio between thermal desorption rate and precursor flux, and the ratio between the typical substrate diffusion distance and beam diameter.

3.4 Continuum model for pulsed irradiation

Also for pulsed irradiation, continuum models can be constructed. Here, we will model the deposition rate for various dwell periods and beam currents. For that purpose, we assume that adsorbed precursor molecules from RZ2 diffuse into RZ1 proportionally to the density of empty

sites ($=n_0 - n$) in RZ1. RZ1 is a circular region around the beam impact point with radius r. We assume that in RZ1 primary ions and SE1's are the only energetic particles. Furthermore, we assume that apart from diffusion, only decomposition and beam-induced desorption take place; thus, adsorption and thermal desorption are neglected.

We define:

$$\sigma_1^* \equiv \sum_{i(\mathrm{RZ1})} \sigma_i^{\mathrm{eff}} \frac{f_i(\vec{r},t)}{f_{\mathrm{PI}}(\vec{r},t)} = \sigma_{\mathrm{PI}}^{\mathrm{eff}} + \eta_{\mathrm{SE1}} \sigma_{\mathrm{SE1}}^{\mathrm{eff}}, \tag{11}$$

where η_{SE1} is the number of generated SE1's per primary ion. From Eqs. (2) and (11) follows:

$$q_1 = \sigma_1^* f_{\mathrm{PI}} n, \tag{12}$$

where q_1 is rate of depositions per unit area in RZ1. Note that $g_1 = V_p q_1$ is the vertical growth in nm/µs.

The desorption rate per unit area is:

$$d_1 = \sigma_{\mathrm{des}}^* f_{\mathrm{PI}} n, \tag{13}$$

where σ_{des}^* is the effective desorption cross section. Integration over the beam profile A gives:

$$\begin{aligned} Q_1 &= \int_A q_1 \mathrm{d}A = \sigma_1^* \int_A f_{\mathrm{PI}} n \mathrm{d}A \quad \text{and} \\ D_1 &= \int_A d_1 \mathrm{d}A = \sigma_{\mathrm{des}}^* \int_A f_{\mathrm{PI}} n \mathrm{d}A. \end{aligned} \tag{14}$$

Now, we assume that rapid diffusion within RZ1 removes all spatial variations in n. Thus:

$$\begin{aligned} Q_1 &= \sigma_1^* n \int_A f_{\mathrm{PI}} \mathrm{d}A = \sigma_1^* F_{\mathrm{PI}} n \quad \text{and} \\ D_1 &= \sigma_{\mathrm{des}}^* n \int_A f_{\mathrm{PI}} \mathrm{d}A = \sigma_{\mathrm{des}}^* F_{\mathrm{PI}} n. \end{aligned} \tag{15}$$

In reality, the flux distribution of the SEs f_{SE1} differs from the flux distribution, or beam profile, f_{PI} of the primary ions. However, the assumption that in RZ1 local differences in density n are absent and the integration over the primary beam profile nullify any effects due to differences between both flux distributions.

Thus, the change in the average density n of precursors in RZ1 is:

$$\frac{\mathrm{d}n}{\mathrm{d}t} = -\frac{Q_1}{\pi r^2} - \frac{D_1}{\pi r^2} + \beta(n_0 - n), \tag{16}$$

where β is a proportionality constant, depending on the precursor diffusion into RZ1. From Eqs. (15) and (16) follows the differential equation

$$\frac{\mathrm{d}n}{\mathrm{d}t} = -\frac{\sigma_1^* + \sigma_{\mathrm{des}}^*}{\pi r^2} F_{\mathrm{PI}} n + \beta(n_0 - n) \equiv -\alpha F_{\mathrm{PI}} n + \beta(n_0 - n) \tag{17}$$

with the solution

$$n(t) = \left(n_0 - \frac{\beta n_0}{\alpha F_{\mathrm{PI}} + \beta}\right) \mathrm{e}^{-(\alpha F_{\mathrm{PI}} + \beta)t} + \frac{\beta n_0}{\alpha F_{\mathrm{PI}} + \beta}. \tag{18}$$

Note that at the beginning of a dwell period ($t = 0$), the density is n_0. The total volumetric growth Γ_1 in RZ1 during the entire dwell time τ_{d} is:

$$\begin{aligned} \Gamma_1 &= V_{\mathrm{p}} \int_0^{\tau_d} Q_1(t) \mathrm{d}t = V_{\mathrm{p}} \sigma_1^* F_{\mathrm{PI}} \int_0^{\tau_d} n(t) \mathrm{d}t \\ &= V_{\mathrm{p}} \sigma_1^* F_{\mathrm{PI}} n_0 \left[\left(1 - \frac{\beta}{\alpha F_{\mathrm{PI}} + \beta}\right)\left(\frac{1 - \mathrm{e}^{-(\alpha F_{\mathrm{PI}} + \beta)\tau_d}}{\alpha F_{\mathrm{PI}} + \beta}\right) + \frac{\beta \tau_d}{\alpha F_{\mathrm{PI}} + \beta}\right]. \end{aligned} \tag{19}$$

The growth Δh in height per ion is:

$$\begin{aligned} \Delta h &= \frac{\Gamma_1}{\pi r^2 F_{\mathrm{PI}} \tau_d} = \frac{1}{\pi r^2} \frac{V_{\mathrm{p}} \sigma_1^* n_0}{\alpha F_{\mathrm{PI}} + \beta} \\ &\left[\left(1 - \frac{\beta}{\alpha F_{\mathrm{PI}} + \beta}\right)\left(\frac{1 - \mathrm{e}^{-(\alpha F_{\mathrm{PI}} + \beta)\tau_d}}{\tau_d}\right) + \beta\right]. \end{aligned} \tag{20}$$

We will use Eq. (20) later to analyze the pulsed growth of He-IBID pillars [39].

3.5 Computer simulation of He-IBID: the EnvisION code

Because analytical solutions are only applicable in specific situations and because the fundamental processes are qualitatively simple, most progress has been obtained by Monte Carlo simulation. The EnvisION code of Smith et al. [28] is at present the most extensive simulation model for IBID. Since all relevant processes are sequential, simulation on an ion-to-ion basis is relatively straightforward. The ion trajectories are calculated via the SRIM code [29] and the SE production via the IONiSE code [42]. However, the non-steady state, the dependencies of rates on many parameters—sometimes only approximately known—and counteracting processes (sputtering, depletion, deposition) complicate interpretation of simulation results.

Using the EnvisION simulation code with realistic values for the fundamental deposition processes, Chen et al. [38] studied $Pt_{20}C_{80}$ pillar growth by He-IBID. The simulations reproduce the measured current dependences of the vertical, lateral, and volumetric growth rates.

Figure 9 shows simulated pillars for a low (1 pA) and a high (9 pA) current. Note that the range of 25-keV He^+ ions in this material is about 200 nm. The simulation results confirm the notion that the vertical growth is mainly due to SE1 (yellow region) and the lateral outgrowth to SE2 (cyan), whereas the contributions by primary ions (red

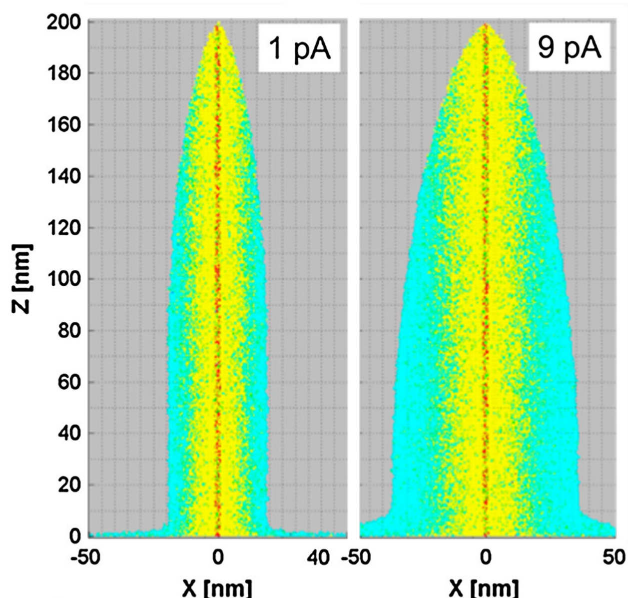

Fig. 9 Cross sections of simulated He-IBID pillars for 1 and 9 pA He^+ current. The *color* codes for the type of particle that caused deposition. From *center* to *rim*: *red* primary ions, *yellow* SE1 electrons, *green* deflected ions, *cyan* SE2 electrons. At 9 pA, lateral growth by SE2 dominates. Reprinted by permission from [38]. Copyright 2010 IOP Publishing

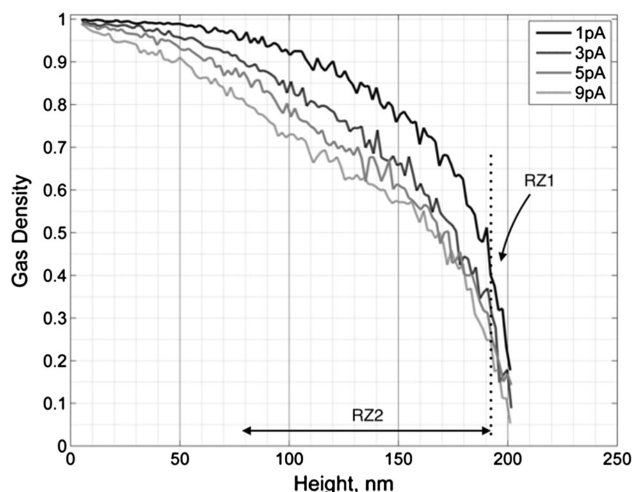

Fig. 10 Simulated relative density *n* of precursors on the pillar surface for various currents. The apex is at 200 nm. Depletion in the primary reaction zone RZ1 is high (>70 %) and in the secondary reaction zone RZ2 typically 20–40 %. Reprinted by permission from [38]. Copyright 2010 IOP Publishing

region) and deflected ions (green) are small. This result is in qualitative agreement with the continuum model of pillar growth sketched above.

Figure 10 shows the simulated surface density *n* of precursors as a function of the height on the pillar [38]. One can see that the precursor density in the primary reaction zone (RZ1) at the pillar apex decreases from 35 % at 1 pA to 15 % at 9 pA. The precursor density in the secondary reaction zone (RZ2) decreases as well, but relatively less, typically from 80 to 60 %. Thus, the apex grows in the precursor-limited regime, whereas the ion-current-limited regime holds for the flanges. As a consequence, the flanges benefit from an increase in current, but not the apex. Figure 10 explains the observed increase in pillar width with increasing beam current.

Recently, Timilsina et al. [43] compared He-IBID with Ne-IBID using the same EnvisION code. The simulations predicted narrower pillars for Ne-IBID, which the authors attribute to the smaller interaction volume of Ne ions. This conclusion is, however, not consistent with the broad Ga-IBID pillar of Fig. 6a. Since gas-field Ne^+ ion sources have recently become available, we expect that experiments will settle this controversy soon.

4 Experimental studies of He-IBID

4.1 Application of He-IBID for modification of a photonic crystal

The maximum beam current the Orion HIM can deliver is 100 pA, although a sub-nanometer beam probe is obtained

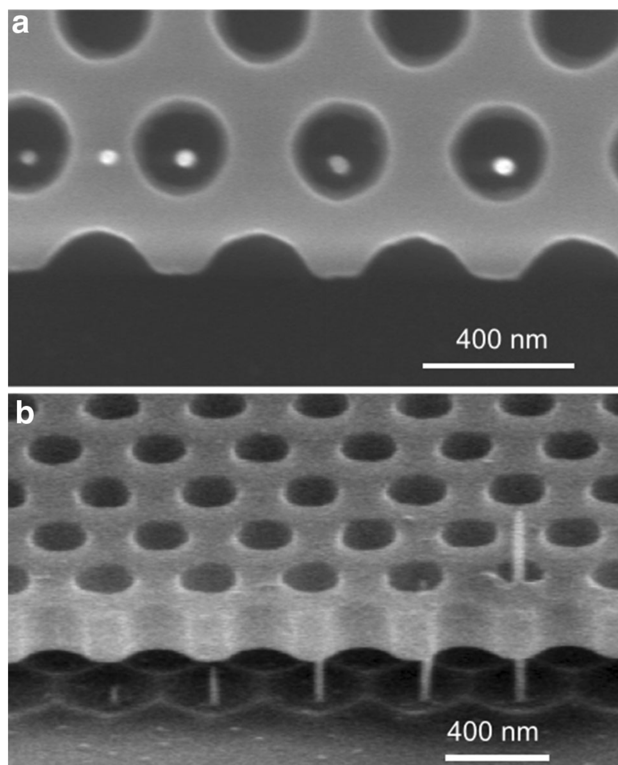

Fig. 11 He-IBID pillars of PtC_x grown in a suspended photonic crystal. **a** Top view, **b** bird's-eye view [44]

only with currents of at most a few picoamperes. Hence, high-volume deposition is impracticable. Nevertheless, the high spatial precision and the minimal proximity effects make He-IBID very useful for specific applications. Figure 11 is an example in which the dielectric constant of a few holes in a suspended photonic crystal is changed by growing a pillar near the center of the hole. Note that there is no visible deposition outside the pillars.

4.2 Volumetric growth rate or deposition efficiency

In various studies, the deposition efficiency for the growth of PtC_x boxes from $MeCpPtMe_3$ has been measured [16, 21, 45, 46], the efficiency being defined as the growth in volume per ion or charge unit. Chen et al. [38] measured the deposition efficiency for Pt pillar growth and Kohama et al. [47] for tungsten pillars. Figure 12 summarizes the results of these studies.

Despite variations in experimental conditions, clear and consistent trends are noticeable. In general, the growth rate decreases with increasing beam current from ~0.1 nm^3/ion near 0.2 pA [45] to ~0.01 nm^3/ion at 20 pA [46]. Assuming a density of 11 PtC_4 'molecules' per nm^3 [38], the deposition yield is between 0.1 and 1 Pt atom per He^+ ion. Surprisingly, the deposition efficiencies for the pillar and the boxes do not differ noticeably.

Kohama et al. [47] grew W pillars. For 30-keV He^+, they found values between 0.01 nm^3/ion at 0.2 pA and 0.002 nm^3 at 4 pA. But at 0.1 pA, the deposition efficiency was considerably higher: 0.035 nm^3/ion. (Note: for clarity, the W data in Fig. 12 have been multiplied by 10, except the one at 0.1 pA.) Although these values are about an order of magnitude lower than for Pt deposition, the current dependencies of the growth rates for Pt and W are similar.

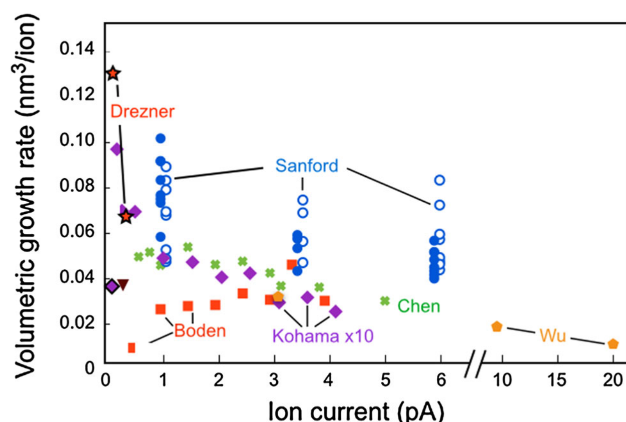

Fig. 12 He-IBID deposition efficiencies in terms of deposited volume per incident ion for growth of PtC_x from $MeCpPtMe_3$ [16, 21, 38, 45, 46] and W from $W(CO)_6$ [47]. The *purple* data points for W have been multiplied by 10, except the first (*black-purple diamond*) at 0.1 Pa

Unfortunately, the precursor fluxes are not known, and therefore, it is not clear whether a lower reaction cross section, a lower SE yield, or a lower precursor supply is responsible of the observed low deposition efficiency for W.

Deposition yields for He-IBID and Ga-IBID are comparable. For instance, Tao et al. [48] measured a yield of 2.5 Pt atoms per Ga^+ ion of 32 keV at normal incidence, and Puretz and Swanson [49] found a growth rate for 25 keV Ga^+ of 0.08 nm^3/ion. Dubner et al. [50] and Ro et al. [32] measured the deposition yield of gold from dimethyl goldhexafluoroacetylacetonate [DMG(hfac)] for 2–100 keV He^+, Ne^+, Ar^+, Kr^+, and Xe^+ ions. They observed that the measured decomposition yield scales with the ion's nuclear energy loss and therefore concluded that the mechanism of precursor decomposition is excitation by energetic surface atoms, produced in the collision cascade. As mentioned in the Sect. 2.1, the nuclear energy loss of He^+ in Si is more than 100 times lower than of Ga^+. From the comparable yields of Pt deposition and the huge difference in nuclear energy loss, we conclude that the collision-cascade or energetic-surface-atom model is not the mechanism of He-IBID. Alternative explanations are thermal activation or excitation by SEs, produced via the electronic energy loss of the He^+ ions. However, thermal activation is unlikely because isolated tall pillars and low boxes have similar deposition efficiencies, but very different heat conductance.

4.3 Deposition with a pulsed beam

Precursor depletion slows down growth. Depletion occurs mainly in the primary reaction RZ1 around the beam impact site, but also to a lesser extent in a wider zone (see Fig. 10). In order to avoid depletion without reducing the ion current, it is best to use a scanning or a pulsed beam [39]. The beam exposes a site for a finite time; then, it is either interrupted or moved to another site, and after a specified time returns to the original site. This procedure is repeated many times. When the beam returns, adsorption and/or diffusion should have replenished the depleted precursor molecules.

The first ion in a new dwell period arrives when the precursor density is at a maximum. For successive ions, the density drops continuously. The speed of the drop depends on the number of precursors nearby the beam impact point—in practice the primary reaction zone RZ1—and by the cross sections for beam-induced decomposition and beam-induced desorption. Figure 13 shows measurements of the pillar growth rate for various beam currents. Clearly, the rate decreases with increasing number of ions per dwell period. Diffusion into RZ1 counteracts the dropping number of precursors, and a balance between precursor influx

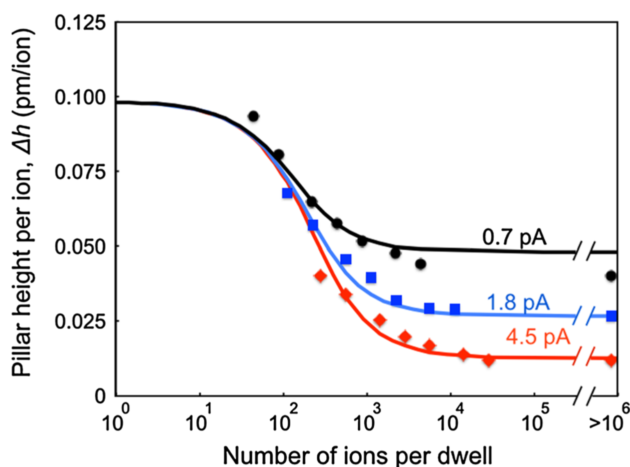

Fig. 13 Increase of Pt-pillar height Δh per ion as a function of the number of ions per dwell period for a pulsed beam at various beam currents. Full *curves* are fits to the model discussed in the text. Refreshment time is at least 10 ms. The data points at '>10^6' are for a continuous beam

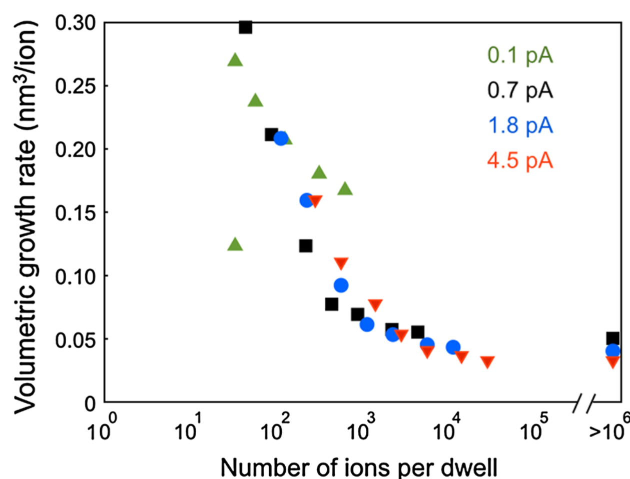

Fig. 14 Deposition efficiency or volumetric growth rate as a function of the number of ions per dwell period for various beam currents. The data points at '>10^6' are for a continuous beam. Reprinted with permission from [39]. Copyright 2011 American Vacuum Society

by diffusion—mainly from RZ2 into RZ1—and precursor consumption is established. Note that since RZ1 is small and the dwell time short, the contribution to replenishment by direct precursor adsorption is negligible.

In the previous section, a model was constructed for deposition with a pulsed beam. Equation (20) describes the growth of the pillar per ion as a function of the number of ions per dwell period. There are three unknown parameters: (1) the decomposition cross section σ_1^*; (2) the number α of precursors lost per ion; and (3) the rate β at which precursors arrive via surface diffusion. For r, the radius of the primary reaction zone RZ1, we take the radius of curvature of the pillar apex, r_c: 9 nm; for the initial precursor density n_0, the literature value of 1.9 $MeCpPtMe_3$ precursors/nm^2 [33]; and for the volume V_p, we take 0.091 nm^3/Pt atom [38]. The full curves in Fig. 13 are the fit results with $\sigma_1^* = 0.14$ nm^2, $\alpha = 0.0064$/ion, and $\beta = 0.027$/µs. The effective deposition cross section σ_1^* is more than one order magnitude larger than the cross section for decomposition by low-energy electrons, as measured by Van Dorp et al. [51], suggesting a yield of approximately 15 SE1's per ion. The inverse of α (155 ions) is the number of ions that removes a full layer of $MeCpPtMe_3$ precursors. Furthermore, from α and σ_1^* follows σ_{des}^* $(=\alpha\pi r_c^2 - \sigma_1^*)$: 1.49 nm^2, which implies that ten times as many precursors are lost by beam-induced desorption than by decomposition. Finally, one can regard β^{-1} (37 µs) as the time needed to fill RZ1 with precursors by diffusion from the surrounding areas. Via $4D\beta^{-1} = r_c^2$, we find a diffusion constant D of 5.4×10^{-9} cm^2/s.

For very short dwell times, Eq. (20) reduces to

$$\Delta h_0 \equiv \Delta h(\tau_d \to 0) = \frac{V_p \sigma_1^* n_0}{\pi r_c^2}. \tag{21}$$

Thus, for the first tens of ions in a dwell period, the pillar growth Δh_0 is 0.098 pm/ion (see Fig. 13), and the volumetric growth is $\Delta V_0 = \Delta h_0 \pi r_c^2 = 0.025$ nm^3/ion. This value is lower than that for the pillars in Fig. 12 (green crosses), because the latter data include lateral outgrowth in RZ2 as well. Finally, the deposition yield Y_d $(=\Delta V_0/V_p)$ is 0.28 Pt atoms per ion.

For $\tau_d \to \infty$, we derive from Eq. (20)

$$\Delta h_\infty \equiv \Delta h(\tau_d \to \infty) = \frac{V_p \sigma_1^* n_0}{\pi r_c^2} \frac{\beta}{\alpha F_{PI} + \beta} = \Delta h_0 \frac{1}{\alpha F_{PI}/\beta + 1}. \tag{22}$$

If $\alpha F_{IP} \gg \beta$, depletion is large and the growth rate is determined by diffusion into the reaction zone; this is, thus, the diffusion-enhanced precursor-limited regime. If $\beta \gg \alpha F_{IP}$, there is negligible depletion and the growth is in the current-limited regime.

Figure 14 shows the volumetric growth per ion as a function of the number of ions per dwell period. The data points for the various currents lie almost on a single curve, up to about 10^4 ions, corresponding to approximately 1-ms dwell time at 1.8 pA. Thus, the amount of precursor conversion depends only on the number of ions per dwell period and not on the length of that period. Of course, if one increases the dwell time without changing the number of ions, there is more time for diffusion. Hence, the balance in conversion shifts from the flanges (RZ2) to the apex (RZ1), and the pillar becomes higher and narrower. This shift is indeed observed [39]. We note that for dwell

times <1 ms, diffusion from outside both reaction zones and direct adsorption from the gas phase are too little to bring substantial quantities of precursors to the apex.

If there is a low number of ions per dwell period, then the deposited volume per ion is large. The data points below 100 ions per dwell continue to increase with decreasing number of ions, whereas one expects a leveling off. It is not clear whether this effect is an artifact related to problematic beam steering at high frequencies, inaccurate beam current measurement at low currents, or adsorption and diffusion of multilayers of $MeCpPtMe_3$ or contamination gases. The highest value in Ref. [39] is 0.8 ± 0.3 nm^3/ion for a 0.1 pA beam at 6 ions/dwell time (not shown in Fig. 14). This value is about one order of magnitude higher than for the growth of boxes of Fig. 12. However, these voluminous pillars were relatively broad, about 90 nm. The low current and short dwell time might have caused instabilities or inaccuracies in the positioning and focusing of the ion beam, thus spreading the primary reaction zone over a larger area and, thus, reducing depletion.

To conclude: the analysis of the pulsed growth of Pt pillars shows that typically 150 He^+ ions remove—either by beam-induced desorption or by decomposition—a Pt precursor layer in the semi-spherical primary reaction zone around the beam impact point. This zone has a radius of about 9 nm. Precursor replenishment into this zone by surface diffusion from the pillar's flange occurs typically within 40 μs. Furthermore, the deposition yield in the current-limited regime is about 0.25 Pt and 1 C atom per ion. Note that on flat surfaces, the escape of SE1's is more difficult, and therefore, the radius of the primary reaction zone might be much smaller.

4.4 Effect of variable refresh time

Long dwell times will not only cause precursor depletion in the reaction zone, but also in a wider area. Steady-state precursor conversion is then only possible if there is refreshment by adsorption. In Fig. 15, the pillar height for a fixed total charge is shown as a function of the refresh time, i.e., the time between the end of one dwell period and the start of the next one at the same site. Alkemade et al. [39] concluded that there are two mechanisms of precursor supply discernible.

The beam dwell time was 100 μs and the current 4.5 pA. Thus, there were 2,800 ions/dwell period, resulting in extensive depletion in the reaction zone. The total charge was 6 pC. Figure 15 shows that a refresh time of about 100 μs (phase I) is sufficient to undo the depletion in the growing apex region, consistent with the value of β^{-1} (37 μs) found in the analysis of Fig. 13. For refresh times between 0.2 and 2 ms (phase II), the deposition rate is independent of refresh time. Likely, diffusion in this time period annuls the

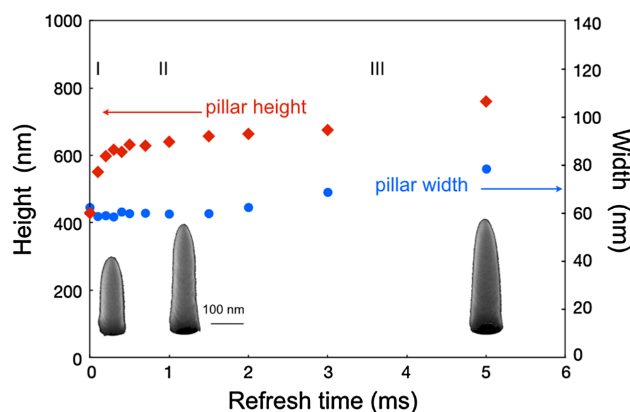

Fig. 15 Pillar height and width as functions of the refresh time. Images of three typical pillars are shown at their respective refresh times. Three phases can be discerned: *I* a short refreshment enhances vertical growth and slightly reduces the pillar width as compared to no refreshment, *II* the height and width of the pillars are not affected by small changes in the refresh time, *III* both height and width increase with refresh time. Reprinted with permission from [39]. Copyright 2011 American Vacuum Society

differences in precursor densities in RZ2. Indeed, for the diffusion constant found in the analysis of Fig. 13 ($D = 5.4 \times 10^{-9}$ cm^2/s), the diffusion distance after 1 ms is approximately 50 nm, consistent with the simulated precursor distribution in Fig. 10. Finally, refresh times longer than 2 ms lead to additional growth. The authors concluded that precursor adsorption on the apex (RZ1) and the nearby flanges (RZ2) starts to contribute to the refreshment in phase III.

4.5 Scan strategy

Refreshment is also important for the growth of broad structures, e.g., boxes. In that case, the beam resides a short dwell time τ_d in a cell inside the area of the box and subsequently steps to a neighboring cell. When the entire area has been covered, the beam returns to the first cell. There are two confliction requirements for choosing the best beam step size. First, the step size should be small, so that the final surface of the deposit will be smooth. Second, the step size should be larger than the depletion zone; otherwise, growth in one cell is hindered by growth in the previous cell. These conflicting requirements can be accommodated if the order of beam stepping is not simply sequential. A better strategy is interlacing. For instance, every other cell is skipped in the first cycle; and in the second cycle, only the skipped cells are visited. In Fig. 16a, the conventional scanning order for 64 cells is shown and an interlacing order in Fig. 16b. In the latter approach, every other column and every other row are skipped, and after four cycles, the beam returns to the first cell. Red circles denote the depletion zones. In the conventional beam stepping order, depletion zones overlap, which

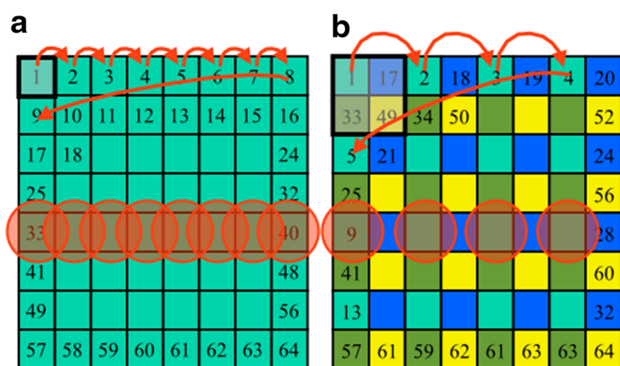

Fig. 16 Beam scanning strategies. In **a,** the beam steps from one cell to its neighboring cell (see *red arrow*); in **b,** interlacing is used. The *red circles* denote the depletion zones; in **a,** they overlap, reducing the total growth rate; in **b,** there is no overlap and the growth rate is maximal

reduces the overall growth rate. In the interlacing order, there is no overlap, and the growth rate is maximal.

Recently, Plank et al. [52] have explored the effect of interlacing on PtC_x box growth by EBID. Figure 17a shows the result. A beam step size of 13 nm was sufficiently small to realize boxes with smooth surfaces. However, in order to avoid reduction in growth rate by depletion, the interlace step size had to be at least 100 nm. The optimal scan strategy resulted in an 80 % higher growth rate than the conventional strategy.

Miro and Alkemade [53] performed a similar experiment for He-IBID using a 0.3-pA and 25-keV He^+ beam with a probe size of about 1 nm. The minimal step was 4 nm, and the interlace step size multiples of 4 nm. The dwell time τ_d was 16 µs, corresponding to 30 ions per dwell period, whereas the cycle time was 66 ms. The substrate was silicon. The outcome of the He-IBID experiment was very different (see Fig. 17b). The growth rate at the largest interlace step size of 32 nm was barely 10 % higher than at the smallest of 4 nm. Thus, in He-IBID, the depletion zone is more than an order of magnitude smaller than in EBID.

Figures 16 and 17b lead to the interesting conclusion that depletion in He-IBID is relatively simple. Within certain limits, beam scanning parameters—such as dwell time and step size—affect the growth only indirectly. The important parameters are the number of ions per dwell period and the refresh time.

5 Characterization of He-IBID material

5.1 Microstructure and composition of He-IBID deposits

Trimethyl (methylcyclopentadienyl)-platinum, $MeCpPtMe_3$, is a very common precursor for metal deposition in EBID

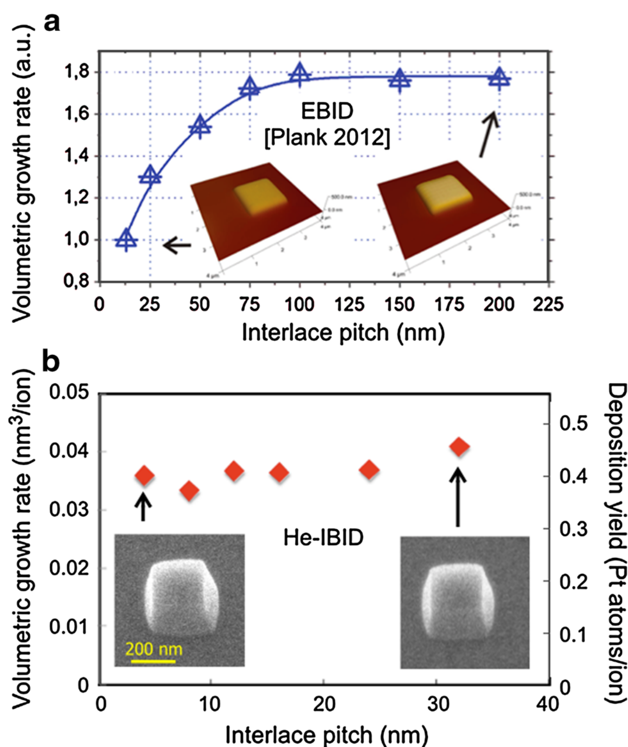

Fig. 17 Volumetric growth rates as a function of interlace pitch for **a** EBID and **b** He-IBID. *Insets* show **a** AFM and **b** HIM images of typical boxes. **a** Reprinted with permission from [52]. Copyright 2012 American Chemical Society. **b** From Ref. [53]

and IBID. However, the deposited material is not at all pure platinum. For Ga-IBID, Pt atomic concentrations are typically between 30 and 40 %; the rest is mainly C, Ga, and an unknown quantity of H [33, 54]. For EBID, Pt concentrations are between 10 and 20 %, and the rest is mainly C, some O, and maybe H.

Sanford et al. [21] measured with energy dispersive spectroscopy (EDS) the composition of He-IBID deposits for this precursor and found concentrations between 8 and 20 %, very similar to EBID. The authors performed of statistical design-of-experiments (DOE) in order to trace the parameters that influence the composition. They found a negative correlation between Pt concentration and deposition yield and a positive correlation between Pt concentration and current.

Drezner et al. [45] made and analyzed TEM lamellae of tall (1.0–1.8 µm) and wide (280 nm) Pt pillars. They used a low (0.35 pA) and a very low (0.1 pA) He^+ current. For 0.35 pA, they measured Pt concentrations of 10–20 %, similar to Sanford et al. [21] and Wu et al. (16 %) [46]. For 0.1 pA, however, they found Pt concentrations twice as high (see Fig. 18). The highest concentration was at the top of the pillar. The authors presume that the lower current allowed more time for methane to form and desorb, lowering the C content of the deposit. Moreover, the growth rate at 0.1 pA

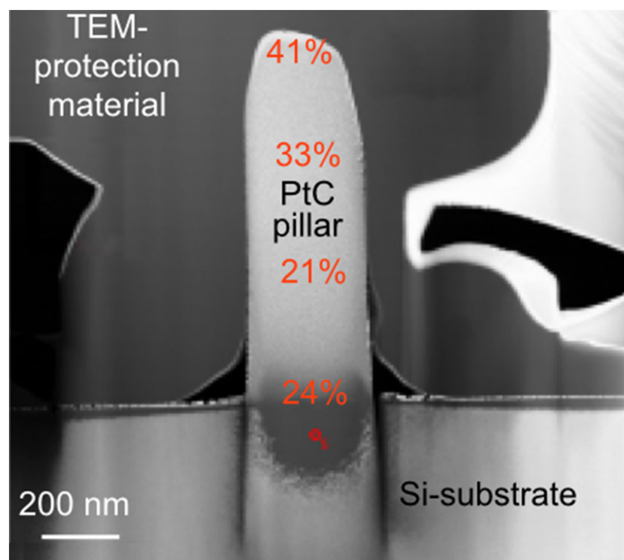

Fig. 18 Cross section of a Pt pillar, grown by IBID of $MeCpPtMe_3$ with a 25-keV and 0.1-pA He^+ beam. The beam was scanned in a 200-nm-wide box. The Pt contents, measured with TEM-EDS, at various heights are indicated. The *dark and bright regions* around the pillar are protection material for the cross sectioning. Below the pillar there is a 200-nm-thick defected zone, caused by He implantation during the first phase of the deposition. Reprinted with permission from [45]. Copyright 2012 American Vacuum Society

was high: 0.13 nm^3/ion (see Fig. 12). The decreasing C concentration toward the top might be due to an increase in temperature with increasing height during the growth.

In the Si material below the base of the pillars, many defects are present, caused by He^+ implantation. Details of defect formation in Si by He^+ implantation can be found in Ref. [35]. The high-resolution TEM image of Fig. 7a reveals the deposit's microstructure: Crystalline Pt grains embedded in a carbonaceous matrix, with grain sizes of 2.4 ± 0.4 nm. An enlargement of Fig. 7a is shown in Fig. 22a. In this pillar, the average Pt composition was about 18 %, as measured with EDS. Wu et al. observed a very similar structure (see Fig. 21a), though with slightly larger grains, typically 3.2 ± 0.35 nm [46]. Also for EBID, similar microstructures have been observed in PtC_x pillars, see Fig. 22b [55].

Kohama et al. [47] grew tungsten pillars via He-IBID decomposition of $W(CO)_6$ and studied their microstructure and composition. The pillars consisted of face-centered cubic WC_{1-x} and/or $W_2(C,O)$ grains for all deposition conditions. Figure 19 shows TEM images of a few pillars. The tungsten pillars had a width of 40 nm and a height of up to 2 μm. The authors concluded that the volumetric growth rate determined the microstructure of the pillars. Previously, Hill and Faridur Rahman [6] grew a 6.5-μm-long and 50-nm-wide W pillar. Columnar voids with a width of 1–15 nm are found in the center of the pillars of

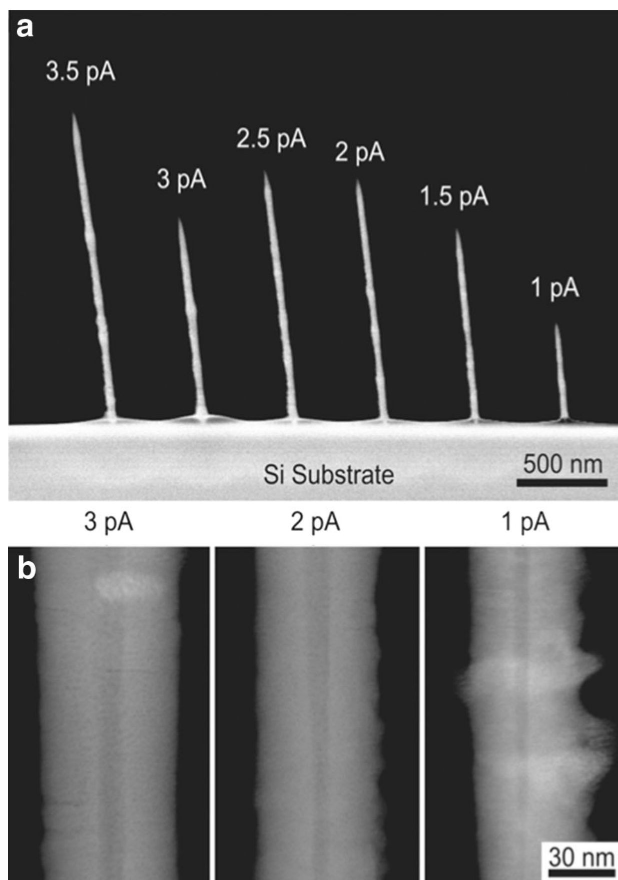

Fig. 19 **a** Tungsten pillars, grown by IBID from $W(CO)_6$ with a stationary 30-keV He^+ beam at various currents. Exposure time is always 60 s. Note that the pillars in **b** are hollow. Reprinted with permission from [47]. Copyright 2013 American Vacuum Society

Fig. 19b. According to the authors, the presence of voids suggests that the pillars are continuously being sputtered by the incident He^+ beam. The narrowest voids are observed for the lowest currents, indicating that hindrance of precursor delivery to the center of the reaction zone is involved in void formation as well. We note that dips in the center of EBID deposits have been observed and explained by Utke et al. [41]. Chen et al. [56] used the balance between sputtering and deposition to make narrow pores in the center of Ga-IBID deposits.

The microstructure of He-IBID grown cobalt [57], see the left inset of Fig. 20, is very different. The metal is almost pure and consists of small, filament like crystallites.

5.2 Resistivities

Electrical contacts in micro- or nanoscale devices can be made via deposition of metallic material. Although IBID and EBID are very powerful in terms of spatial precision, the quality of the deposited material is often poor. For instance, pure platinum has a resistivity of 10 μΩ cm. In

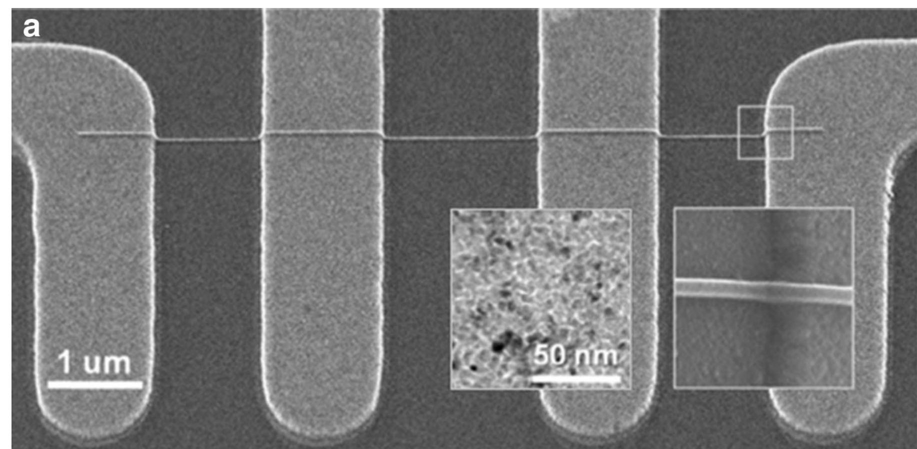

Fig. 20 HIM image of a 30-nm-wide Co line grown by He-IBID on top of four Au electrodes. The *left inset* is a bright-field TEM micrograph of a similar deposit, showing crystallites of about 6 nm; the other *inset* is a HIM magnification showing good step coverage. Reprinted with permission from [57]. Copyright 2014 Springer

EBID, the typical resistivity of the material deposited from $MeCpPtMe_3$ is in the 10^6–10^7 μΩ cm range [54]. By post-deposition anneal in oxygen, Botman et al. [58] achieved 10^4 μΩ cm, with a concurrent increase of the Pt content from 15 to 70 %. However, this effective treatment changes also the shape and volume of the deposit. In Ga-IBID, the same precursor can result in a Pt content above 40 % and a resistivity well below 10^3 μΩ cm [54, 59].

Resistivity measurements for He-IBID material are scarce. First results with $MeCpPtMe_3$ showed the same 10^6–10^7 μΩ cm range as for EBID [23]. Recently, Wu et al. [46] obtained resistivities at room temperature of the order of 10^5 μΩ cm. The best result—3.5×10^4 μΩ cm—was obtained at low beam energy (10 keV) and high currents (above 15 pA). Wu et al. explain the decrease in resistivity to a higher temperature during deposition at the higher current. This explanation is consistent with the study of Sanford et al. [21] that shows a correlation between He^+ current and Pt content.

In a recent study, Wu et al. [57] made 10-nm-wide Co lines by He-IBID with dicobalt octacarbonyl [$Co_2(CO)_8$]. Figure 20 shows one line in a four-point probe test structure. Electrical measurements revealed a resistivity of 50–100 μΩ cm, only one order of magnitude above the bulk value. The purity was high; in particular, the carbon content was less than a few percent, much lower than achievable by EBID [33]. The authors link the low resistivity to the high Co content and the relatively large grains (see the left inset of Fig. 20).

6 Comparison with related techniques

6.1 Comparison with heavy-ion IBID

Qualitatively similar processes take place during IBID with heavy ions. In particular, Ga-IBID has been widely explored and exploited. Yet, there are three important differences between Ga-IBID and He-IBID. First of all, sputtering of atoms from the substrate material and the deposit is prominent for heavy ion beams. If the precursor supply is low, the net growth might be negative, with more substrate sputtering than precursor deposition. In He-IBID, sputtering yields are 10–50 times lower, and therefore, effects of sputtering on the deposits are small or undetectable. The hollow core of the W pillars of Fig. 19 is an interesting exception.

A second difference is the assumed mechanism of precursor excitation. Heavy ions in the tens of keV energy range lose their energy in materials mainly by atomic collisions: Most of their energy is transferred as kinetic energy to recoiled atoms. Experiments by Dubner et al. [50], Tao et al. [48], and Ro et al. [32] suggest that these energetic, or excited, recoils near the surface are responsible for the excitation and subsequent decomposition of adsorbed precursor molecules, see the sketch of Fig. 2b. However, there is indirect evidence that SEs are involved as well [60]. Light ions of the same energy transfer hardly any kinetic energy to recoil atoms; most energy is lost by electronic excitations [29, 30]. Nevertheless, He-IBID and Ga-IBID show comparable deposition yields (see Fig. 6) and the discussion of Fig. 12. Since the mechanism of He-IBID cannot be linked to energetic surface atoms, one must conclude that precursor excitation by SEs is the mechanism of He-IBID.

A third important difference is the width of the reaction zone. First of all, most commercial Ga-FIBs do not have a probe diameter below 5 nm. In addition, the lateral scattering of Ga^+ ions in materials is relatively strong (see Fig. 3). The range and lateral spread of 30-keV Ga^+ ions in a medium-Z material are both typically 20 nm. In contrast, the lateral spread of helium ions in matter is much lower, typically a few nanometers in the outermost 100 nm of material (see Fig. 3). Also the range of low-energy SE's is

only a few nanometers [61]. As a consequence, structures can be made with much better spatial precision with He-IBID than with Ga-IBID, compare, e.g., the pillars of Fig. 6a, b.

6.2 Comparison between Ne-IBID and He-IBID

The newest generation of gas-field ion microscopes of Zeiss can produce focused neon ion beams as well, providing new possibilities for high-resolution nano-fabrication [62, 63]. In a recent publication, Wu et al. [46] investigated neon-beam-induced deposition.

The authors compared IBID growth of platinum wires from $MeCpPtMe_3$ by He^+ and Ne^+ ion beams. Figure 21 shows TEM micrographs of the deposited materials. The He-IBID platinum (a) resembles that of Fig. 7a, although it has slightly larger grains. The grains are clearly larger for Ne-IBID growth: 4.5 ± 0.7 nm. We note that the study by De Teresa et al. [54] showed grain sizes of 3.2 ± 0.8 nm, both for Ga-IBID and EBID. The He-IBID and Ne-IBID deposited materials have comparable compositions (16 and 17 % Pt, respectively). The room temperature resistivity of the Ne-IBID material was approximately 1,000 μΩ cm, about two orders of magnitude lower than for the He-IBID material. Wu et al. measured also the temperature-dependent conductance. The observed strong drop of the conductance with decreasing temperature in the He-IBID material is consistent with a granular material in the weak intergrain tunneling-coupling regime. The behavior of the Ne-IBID material was very different: There was a small decrease of the conductance with decreasing temperature, indicative of a granular metal in the strong-coupling regime. The authors concluded that the abundant nuclear collisions of the Ne^+ ions in the deposit promote platinum mobility, thus enhancing grain growth and improving the electrical conductance. This mixing mechanism is absent in He-IBID, explaining the high resistivities.

6.3 Comparison with EBID

Sputtering is obviously absent in EBID. A low flux of precursors implies only slow deposition. The mechanism of precursor decomposition is mainly excitation by low-energy SEs. However, there are a few additional important differences between EBID and He-IBID. The SE yield for 30 keV He^+ is typically between 2 and 5 electrons per ion [7], whereas for primary electron beams, it is between 0.1 and 1. Another important difference is the energy of the SEs. For a He^+ beam, almost all SEs have an energy below 10 eV [31]. Sub-10-eV SEs are also abundant for electron beam bombardment, but there is a non-negligible fraction of higher-energy electrons. In fact, electron-beam-bombarded materials emit electrons with all energies between zero and the full energy of the primary beam.

Lateral scattering of primary electrons is relatively large, often hundreds of nanometers (see Fig. 3). SEs with energies higher than 100 eV have a longer range than 10–50 eV electrons, but are also effective in precursor decomposition, either by direct decomposition or by generation of other lower-energy electrons. Consequently, EBID structures are coarser than He-IBID structures. For instance, EBID Pt pillars grown by Plank et al. [55] with the same precursor as in Fig. 7 were at least 100 nm wide. Nevertheless, the apex of the pillars can have comparable sharpness and microstructure, see the TEM micrographs of Fig. 22.

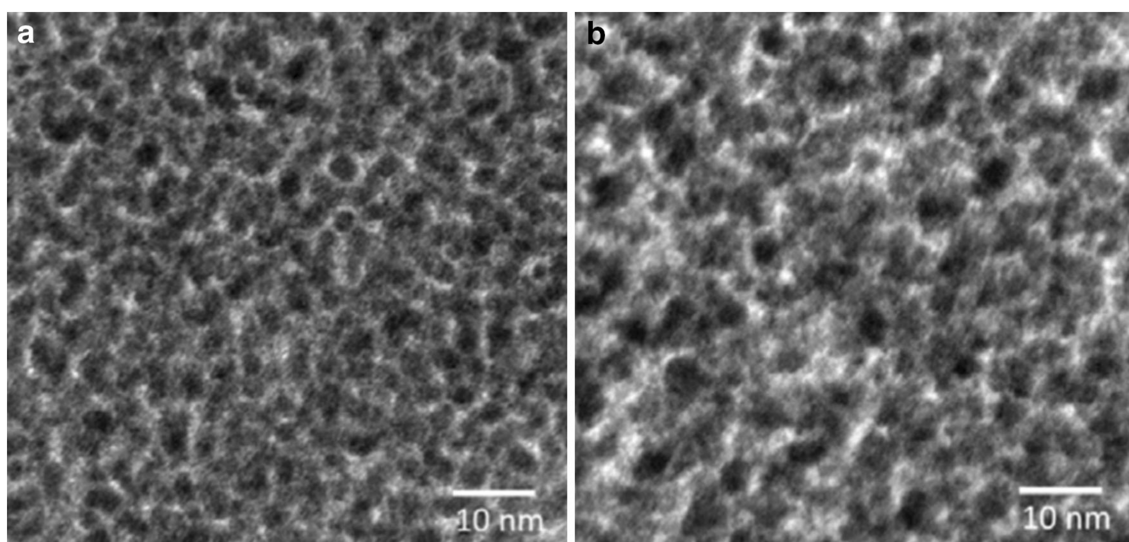

Fig. 21 Transmission electron micrographs of Pt, grown via **a** He-IBID and **b** Ne-IBID. Reproduced by permission from [46]. Copyright 2014 IOP Publishing

Plank et al. concluded that primary electrons and SE1s contributed to growth of the pillar. He-EBID is, thus, not principally different. However, overspray—i.e., growth of a thin deposit in a wide area around the actual deposit—is much more prominent in EBID than in He-EBID. The cause is the much larger scattering of primary electrons (see Fig. 3).

Heavy-ion IBID produces in general purer materials than EBID, because ion beam sputtering can remove additionally nonvolatile precursor fragments, in particular C from metalorganic precursors. In EBID, the composition of the deposit is without further processing often similar to that of the original precursor minus one or two ligands. Because sputtering is weak, the situation for He-IBID is not much different, although optimization of experimental conditions can lead to higher purities (see, e.g., Ref. [45]). In the few materials investigated so far, He-IBID structures have contamination levels between those of EBID and Ga-IBID.

7 Summary and conclusion

The introduction of the Orion gas-field ion microscope by Zeiss in 2006 has opened a new chapter in microscopy. Its highly focused helium ion beam offers sub-nanometer resolution imaging. The Orion allows also for nanofabrication on the nanometer scale. One can either directly remove atoms by He-FIB sputtering, or chemically change resist material, or apply IBID to fabricate structures on the surface of materials.

This chapter presents an overview of the He-IBID work performed on Orion HIMs by various groups during the last 5 years. Since the number of publications is still tractable, we have tried to make this review complete: To our knowledge, we have discussed or at least cited all the work published so far.

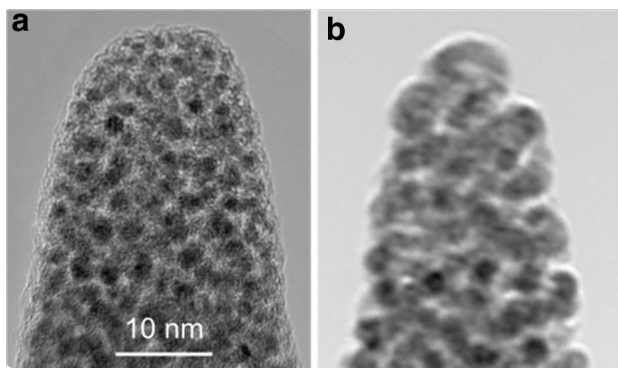

Fig. 22 Transmission electron micrographs of PtC_x grown via **a** He-IBID and **b** EBID [55]. Both images have the same *scale*; **a** an enlargement of Fig. 7a. The *dark* Pt crystallites in both images have the same diameter of 2.5 nm. **a** Courtesy (**a**) Frans Tichelaar, TU Delft. **b** Reproduced by permission from [55]. Copyright 2008 IOP Publishing

Compared with the related techniques of EBID and heavy-ion-beam-induced deposition (usually Ga-IBID), He-IBID takes the intermediate position in some aspects, but in other aspects, it is superior to both. Of course, there are also reasons to choose either EBID or Ga-IBID for specific applications, such as costs (most SEMs are less expensive than a HIM), substrate damage by He^+ implantation, sputter rates and contaminations levels (usually Ga-IBID gives better results), and prior knowledge (still limited for He-IBID).

Most striking is that the composition and microstructure of He-EBID and EBID materials are very similar. Although the deposition yield per primary particle is one or two orders of magnitude higher for a He^+ beam, the yields per SE differ less. The remaining difference might be related to the higher yield of the more effective low-energy SEs (<10 eV) in He^+ bombardment. This similarity and the notion that nuclear energy losses of He^+ in matter are relatively small corroborate the conclusion that low-energy SEs are the major agents in He^+-beam-induced deposition.

Heavy ions of similar energy experience the same electronic energy loss in matter as He^+ ions, but two orders of magnitude larger nuclear energy loss. Yet, deposition yields for He-IBID and Ga-IBID are comparable. Likely, this similarity is a coincidence, because different processes are responsible for the mechanisms of low- and heavy-ion-induced deposition.

The major difference between He-IBID and EBID is the minimal role of proximity effects for the former, a consequence of the weak deflections of He^+ ions traveling in matter. Hence, structures made by He-IBID resemble the movements of the primary beam more than EBID structures do. Therefore, application of He-IBID is in principle easier, and details can be made finer. Moreover, He-IBID is better suited for fundamental analysis of the physical and chemical processes involved. Hence, we expect most progress in fundamental studies to occur in the field of He-IBID. In this work, we applied successfully an analytical model for IBID. The comparison with experimental results yielded quantitative data for precursor diffusion, decomposition, and desorption. Moreover, we showed experimentally that deposition takes place only in a zone of only 5–10 nm in radius around the beam impact point. In other words, proximity effects are minimal. Furthermore, our analysis suggests a prominent role of beam-induced desorption as a cause for precursor depletion during particle beam-induced deposition.

Compared with Ga-IBID, He-IBID is simpler because sputtering is negligible and—once again—because deflections of the ions are weaker. Moreover, there is only one mechanism for precursor decomposition operational. The absence of competing mechanisms reduces the

options for the nanotechnologist to optimize fabrication conditions for dedicated applications, although an interesting exception is the small, but non-negligible effect of sputtering in the center of the beam impact zone, leading to hollow deposits [47]. We conclude that the ability to make structures with high spatial fidelity is the most important asset of He-IBID.

Acknowledgments This work was supported by the Dutch Technology Foundation STW, which is part of the Netherlands Organization of Scientific Research (NWO), and which is partly funded by the Ministry of Economic Affairs.

References

1. J. Gierak, A. Madouri, A.L. Biance, E. Bourhis, G. Patriarche, C. Ulysse, D. Lucot, X. Lafosse, L. Auvray, L. Bruchhaus, R. Jede, Microelectron. Eng. **84**, 779 (2007)
2. C.A. Volkert, A.M. Minor, MRS Bull. **32**, 389 (2007)
3. D. Maas, E. van Veldhoven, P. Chen, V. Sidorkin, H. Salemink, E. van der Drift, P. Alkemade, Proc. SPIE **7638**, 763814 (2010)
4. W.F. van Dorp, Appl. Phys. A (2014). doi:10.1007/s0033901485888
5. V.N. Tondare, J. Vac. Sci. Technol. A **23**, 1498 (2005)
6. R. Hill, F.H.M. Faridur Rahman, Nucl. Instrum. Methods A **645**, 96 (2011)
7. R. Hill, J.A. Notte, L. Scipioni, *Advances in Imaging and Electron Physics*, vol. 170 (Academic Press, New York, 2012)
8. B.W. Ward, J.A. Notte, N.P. Economou, J. Vac. Sci. Technol. B **24**, 2871 (2006)
9. N.P. Economou, J.A. Notte, W.B. Thompson, Scanning **34**, 83 (2012)
10. V. Sidorkin, E. van Veldhoven, E. van der Drift, P. Alkemade, H. Salemink, D. Maas, J. Vac. Sci. Technol. B **27**, L18 (2009)
11. D. Winston, B.M. Cord, B. Ming, D.C. Bell, W.F. DiNatale, L.A. Stern, A.E. Vladar, M.T. Postek, M.K. Mondol, J.K.W. Yang, K.K. Berggren, J. Vac. Sci. Technol. B **27**, 2702 (2009)
12. W.-D. Li, W. Wu, R.S. Williams, J. Vac. Sci. Technol. B **30**, 06F304 (2012)
13. X.-H. Zhang, H. Vieker, A. Beyer, A. Gölzhäuser, Beilstein J. Nanotechnol. **5**, 188 (2014)
14. D.C. Bell, M.C. Lemme, L.A. Stern, J.R. Williams, C.M. Marcus, Nanotechnology **20**, 455301 (2009)
15. A.I. Kuznetsov et al., Nature Comm. **5**, 3104 (2014)
16. S.A. Boden, Z. Moktadir, D.M. Bagnall, H. Mizuta, H.N. Rutt, Microelectron. Eng. **88**, 2452 (2011)
17. S. Tan, R. Livengood, D. Shima, J. Notte, S. McVey, J. Vac. Sci. Technol. B **28**, C6F15 (2010)
18. J. Yang, D.C. Ferranti, L.A. Stern, C.A. Sanford, J. Huang, Z. Ren, L.-C. Qin, A.R. Hall, Nanotechnology **22**, 285310 (2011)
19. D. Fox, Y. Chen, C.C. Faulkner, H. Zhang, Beilstein J. Nanotechnol. **3**, 579 (2012)
20. M. Rudneva, E. van Veldhoven, S.K. Malladi, D. Maas, H.W. Zandbergen, J. Mater. Res. **28**, 1013 (2013)
21. C.A. Sanford, L. Stern, L. Barriss, L. Farkas, M. DiManna, R. Mello, D.J. Maas, P.F.A. Alkemade, J. Vac. Sci. Technol. B **27**, 2660 (2009)
22. D.J. Maas, E.W. van der Drift, E. van Veldhoven, J. Meessen, M. Rudneva, P.F.A. Alkemade, Mater. Res. Soc. Symp. Proc. **1354**, 33 (2011)
23. P.F.A. Alkemade, E. van Veldhoven, in *Nanofabrication*, ed. by M. Stepanova, S. Dew (Springer, Vienna, 2007), p. 275
24. P.F.A. Alkemade, E.M. Koster, E. van Veldhoven, D.J. Maas, Scanning **34**, 90 (2012)
25. B. Singh, AIP Conf. Proc. **1525**, 392 (2013)
26. G. Hlawacek, V. Veligura, R. van Gastel, B. Poelsema, J. Vac. Sci. Technol. B **32**, 020801 (2014)
27. L.E. Ocola, C. Rue, D. Maas, MRS Bull. **39**(336), 336 (2014)
28. D.A. Smith, D.C. Joy, P.D. Rack, Nanotechnology **21**, 175302 (2010)
29. J.F. Ziegler, J.P. Biersack, M.D. Ziegler, *SRIM—The Stopping and Range of Ions in Matter* (SRIM, Chester, 2008)
30. R. Behrisch, W. Eckstein, *Sputtering by Particle Bombardment Experiments and Computer Calculations from Threshold to MeV Energies* (Springer, Berlin, 2007)
31. Y.V. Petrov, O.F. Vyvenko, A.S. Bondarenko, J. Surf, Investigation. X-ray Synchrotron Neutron Tech **4**, 792 (2010)
32. J.S. Ro, C.V. Thompson, J. Melngailis, J. Vac. Sci. Technol. B **12**, 73 (1994)
33. I. Utke, P. Hoffmann, J. Melngailis, J. Vac. Sci. Technol. B **26**, 1197 (2008)
34. J. Notte, B. Ward, N. Economou, R. Hill, R. Percival, L. Farkas, S. McVey, AIP Conf. Proc. **931**, 489 (2007)
35. R. Livengood, S. Tan, Y. Greenzweig, J. Notte, S. McVey, J. Vac. Sci. Technol. B **27**, 3244 (2009)
36. P.F.A. Alkemade, P. Chen, E. van Veldhoven, D. Maas, J. Vac. Sci. Technol. B **28**, C6F22 (2010)
37. P. Chen, PhD dissertation, Delft University of Technology (Casimir PhD-series, Delft-Leiden, 2010)
38. P. Chen, E. van Veldhoven, C.A. Sanford, H.W.M. Salemink, D.J. Maas, D.A. Smith, P.D. Rack, P.F.A. Alkemade, Nanotechnology **21**, 455302 (2010)
39. P.F.A. Alkemade, H. Miro, E. van Veldhoven, D.J. Maas, D.A. Smith, P.D. Rack, J. Vac. Sci. Technol. B **29**, 06FG05 (2011)
40. V. Scheuer, H. Koops, T. Tschudi, Microelectron. Eng. **5**, 423 (1986)
41. I. Utke, V. Friedli, M. Purrucker, J. Michler, J. Vac. Sci. Technol. B **25**, 2219 (2007)
42. R. Ramachandra, B. Griffin, D. Joy, Ultramicroscopy **109**, 748 (2009)
43. R. Timilsina, D.A. Smith, P.D. Rack, Nanotechnology **24**, 115302 (2013)
44. P. Alkemade, in *22nd International Conference on the Applications of Accelerators in Research and Industry* (Fort Worth, 2012)
45. Y. Drezner, Y. Greenzweig, D. Fishman, E. van Veldhoven, D.J. Maas, A. Raveh, R.H. Livengood, J. Vac. Sci. Technol. B **30**, 041210 (2012)
46. H.M. Wu, L.A. Stern, J.H. Chen, M. Huth, C.H. Schwalb, M. Winhold, F. Porrati, C.M. Gonzalez, R. Timilsina, P.D. Rack, Nanotechnology **24**, 175302 (2013)
47. K. Kohama, T. Iijima, M. Hayashida, S. Ogawa, J. Vac. Sci. Technol. B **31**, 031802 (2013)
48. T. Tao, W. Wilkinson, J. Melngailis, J. Vac. Sci. Technol. B **9**, 162 (1991)
49. J. Puretz, L.W. Swanson, J. Vac. Sci. Technol. B **10**, 2695 (1992)
50. A.D. Dubner, A. Wagner, J. Melngailis, C.V. Thompson, J. Appl. Phys. **70**, 665 (1991)
51. W.F. van Dorp, J.D. Wnuk, J.M. Gorham, D.H. Fairbrother, T.E. Madey, C.W. Hagen, J. Appl. Phys. **106**, 074903 (2009)
52. H. Plank, D.A. Smith, T. Haber, P.D. Rack, F. Hofer, ACS Nano **6**, 286 (2012)
53. H. Miro, P. Alkemade, in *European Microscopy Conference* (Manchester, 2012)
54. J.M. De Teresa, R. Córdoba, A. Fernández-Pacheco, O. Montero, P. Strichovanec, M.R. Ibarra, J. Nanomater. **2009**, 936863 (2009)
55. H. Plank, C. Gspan, M. Dienstleder, G. Kothleitner, F. Hofer, Nanotechnology **19**, 485302 (2008)
56. P. Chen, M.-Y. Wu, H.W.M. Salemink, P.F.A. Alkemade, Nanotechnology **20**, 015302 (2009)

57. H. Wu, L.A. Stern, D. Xia, D. Ferranti, B. Thompson, K.L. Klein, C.M. Gonzalez, P.D. Rack, J. Mater. Sci. Mater. Electron. **25**, 587 (2014)
58. A. Botman, J.J.L. Mulders, R. Weemaes, S. Mentink, Nanotechnology **17**, 3779 (2006)
59. T. Tao, J.S. Ro, J. Melngailis, Z. Xue, H.D. Kaesz, J. Vac. Sci. Technol. B **8**, 1826 (1990)
60. P. Chen, H.W.M. Salemink, P.F.A. Alkemade, J. Vac. Sci. Technol. B **27**, 2718 (2009)
61. M.P. Seah, W.A. Dench, Surf. Interf. Anal. **1**, 2 (1979)
62. D. Winston, V.R. Manfrinato, S.M. Nicaise, L.L. Cheong, H.-G. Duan, D. Ferranti, J. Marshman, S. McVey, L. Stern, J. Notte, K.K. Berggren, Nano Lett. **11**, 4343 (2011)
63. C.M. Gonzalez, R. Timilsina, G.-L. Li, G. Duscher, P.D. Rack, W. Slingenbergh, W.F. van Dorp, J.T.M. De Hosson, K.L. Klein, H.M. Wu, L.A. Stern, J. Vac. Sci. Technol. B **32**, 021602 (2014)